Advanced Materials Interfaces

ADVANCED MATERIALS INTERFACES Open Access

www.advmatinterfaces.de

RESEARCH ARTICLE OPEN ACCESS

Polystyrene/TiO_2 Composite Thin Films by Powder Aerosol Deposition: Film Morphology Control Through Powder Processing

Marc C. Thiel[1] | Yannic Wagner[1] | Christoph Pauly[2] | Sascha Verwaayen[3,4] | Markus Gallei[3,5] | Karen Lienkamp[1,5]

[1]Chair of Polymer Materials, Saarland University, Saarbrücken, Germany | [2]Correlative Microscopy and Tomography (CoMiTo) Core Facility, Saarland University, Saarbrücken, Germany | [3]Chair of Polymer Chemistry, Saarland University, Saarbrücken, Germany | [4]Department of Pharmacy, Biopharmaceutics and Pharmaceutical Technology, Saarland University, Saarbrücken, Germany | [5]Saarene, Saarland Center for Energy Materials and Sustainability, Saarbrücken, Germany

Correspondence: Karen Lienkamp (karen.lienkamp@uni-saarland.de)

Received: 30 July 2025 | **Revised:** 16 December 2025 | **Accepted:** 17 December 2025

Keywords: coatings | cold spray | polymer ceramic composites | powder aerosol deposition | thin films

ABSTRACT

Polymer-ceramic composite (PCC) coatings combine functionality with mechanical robustness and flexibility, which is attractive for barrier coatings, membranes, or flexible electronics. Their fabrication is challenging, as conventional ceramic thin film methods make use of polymer-incompatible high-temperature sintering. Powder aerosol deposition (PAD) offers a solvent- and sinter-free avenue toward PCCs. An unresolved key question is how the preparation route of the composite powders dictates the PAD film formation and microstructure. To address this, we investigated PAD deposition of the system polystyrene (PS)-titanium dioxide (TiO_2). PS particles synthesized via emulsion polymerization are combined with TiO_2 particles either through dry mixing, yielding inhomogeneous powders, or through ultrasound-assisted slurry-mixing to form homogeneous powders. When deposited on polycarbonate and steel, these powders produce fundamentally different microstructures, with organized, multilayer-like films emerging from the inhomogeneous powders, and isotropic films from the homogeneous ones. These structural differences correlate with variations in crystallite size revealed by X-ray diffraction, which provided new insights into the role of internal shock absorption of the polymeric component during PAD impact. By employing a sacrificial layer, we obtained free-standing PAD-processed PCC films, which enable accurate compositional determination by thermogravimetric analysis. The fabrication of a 100 cm^2 flexible coating on a PET film illustrates the scalability and potential for barrier and membrane applications. This work provides a transferable blueprint for designing hybrid thin films by PAD with tunable properties, thus bridging between polymer and ceramic processing.

1 | Introduction

Micrometer-thin, functional ceramic coatings, e.g., made from titanium dioxide (TiO_2), aluminum oxide (Al_2O_3), zirconium dioxide (ZrO_2) or silicon carbide, find applications in a variety of fields where surface durability, strength, and hardness as well as thermal and chemical stability are critical. Examples include coatings with high wear and abrasion resistance (e.g., cutting tools, engine components) [1–3], thermal barrier coatings (e.g. gas turbines, spacecraft components) [4–6], electrically insulating coatings (e.g. circuit boards, microchips, micro-electro mechanical systems (MEMS)) [7–9], corrosion-protection coatings (e.g. pipelines, chemical plants) [10–12], selective barrier layers (e.g. separation membranes) [13–15], and coatings for medical devices

(e.g. implants, surgical tools). In these applications, the ceramic layers, which generally have a low toughness, are mechanically stabilized by their underlying substrates [16–18].

Free-standing thin layers of ceramics or flexible, thin ceramic layers as parts of multilayer systems would be promising materials for flexible electronics, transparent flexible dielectrics, MEMS, barrier layers or filtration membranes. Currently, these applications are limited by the low flexibility and high brittleness of ceramics, and in the case of multilayer systems, often also by a low substrate adhesion under tensile or shear stress. Only a few examples of thin, free-standing ceramic and ceramic composite films exist [19, 20]. These include 0.2–3 μm thick Al_2O_3 and yttria-stabilized ZrO_2 obtained by green film spin coating and subsequent sintering or hot-pressing [19], or 100 nm thick TiO_2/poly(acrylic acid) composite films [20]. In these examples, a base layer consisting of a soluble polymer was used as a sacrificial layer, onto which the ceramic precursor layer was deposited. The system was then either sintered at high temperatures to pyrolyze the polymer, so that the ceramic layer would detach [19], or the thermal treatment was limited to a lower temperature range, so that the half-sintered film could be removed by dissolution of the sacrificial layer, and then heated further [20].

Polymer-ceramic composite (PCC) films with a high ceramic content can be promising alternatives to pure ceramic layers for the above-mentioned applications, as they combine the beneficial material properties and functionality of a ceramic component with the flexibility and ductility of polymers. A limiting factor for making thin polymer ceramic composite coatings, especially free-standing ones, are the available processing methods. Conventionally, ceramic coatings are obtained by a combination of a sol–gel process and sintering [7], by physical vapor deposition [6, 21], by electrodeposition [22], or by thermal spray methods [5]. Besides intrinsic problems in the fabrication of multilayer materials by these methods (e.g., coating defects due to incomplete melting, or loss of adhesion due to mismatching thermal expansion coefficients of the coating material and the substrate), these high-temperature processes are incompatible with polymers, which often start to decompose around 300°C. Polymer coatings, on the other hand, are mostly deposited from solution or obtained by melt processing. This either requires organic solvents and can yield defects related to dewetting phenomena (e.g., pinhole formation), and/or the ceramic particles must be surface-modified to prevent aggregation. Additionally, the ceramic particle content is limited as it increases the viscosity of the mixture and may cause too high wear of the fabrication equipment.

In this context, powder aerosol deposition (PAD), a solvent-free spray technique in which particles are deposited at ambient temperature, is an interesting alternative. PAD is typically used for depositing ceramics to obtain thin, nanocrystalline films without the need for sintering [23, 24]. In a typical PAD set-up, ceramic particles are accelerated to high speeds (100–600 m s^{-1}) through pressure differences in the set-up and collide with a target substrate, as illustrated and explained in Figure 1 [24, 25].

Upon collision with the substrate, the ceramic particles fracture and undergo plastic deformation. Film formation generally proceeds through an initial "anchor layer formation" phase, while continued impacts of subsequent particles ("hammering effect") lead to growth and densification of the film, which can reach up to 95% of the theoretical material density without altering the crystal structure of the ceramics [23, 24]. This is referred to as the "room temperature impact consolidation" (RTIC) mechanism [23]. Although the exact mechanistic details are still under debate [24–26], it is widely accepted that PAD operates within a specific deposition window, defined by a lower and an upper critical particle velocity [24, 25]. PAD studies with ceramic powders have shown that both the native properties of the powder (i.e., crystallite size, particle size, and morphology) and its pretreatment (i.e., sieving, drying, preheating, and milling) are critical for the film quality and deposition efficiency [27–37]. Process parameters (i.e., carrier gas type and flow rate) [38–45], as well as characteristics of the substrate (i.e., roughness, hardness, and substrate temperature) have been likewise studied [28, 46–48].

Fabrication of pure polymer films by PAD is underexplored but can be a valuable alternative for poorly soluble or infusible polymers, or other situations where solution- or melt-processing is not viable. By co-depositing polymer and ceramic particles, PCC thin films with variable composition can be fabricated [32, 49–64]. For example, poly(ethylene glycol) or poly(vinylidene fluoride) was used as a sacrificial phase in PCCs, which were then pyrolyzed to yield a porous ceramic layer [49, 50, 53, 56]. In other systems, the polymer content (e.g., poly(tetrafluoroethylene), poly(vinylidene fluoride), polyethylene, poly(methyl methacrylate), or polyimide) in the target PCCs was used to tune dielectric behavior [32, 51, 52, 55, 57, 58], or to increase surface hydrophobicity [63, 65].

There are only a few available fundamental studies of PCC films obtained by PAD. These demonstrate that the films had less residual stress than the corresponding pure ceramic films [51, 58], and that the surface roughness and microstructure of the top layer could be modified [59, 62, 63, 65, 66]. An increase in crystallite sizes in the ceramic phase of PCCs was also observed—a consequence of the polymer phase dissipating parts of the particles' kinetic energy by deformation instead of fracturing upon collision with the substrate [32, 51–53, 55, 57, 59–61, 63, 65, 67]. This is referred to as the "cushion" or "shock-absorption" effect [51, 68].

While these studies demonstrate that PCCs produced via PAD are promising as thin coatings with tailored material properties and good substrate adhesion, a fundamental understanding of how the initial powder characteristics influence the film morphology, properties, and deposition mechanism is lacking. In fact, obtaining suitable polymer powders for PAD is non-trivial, which is a major reason for the current limited amount of work on PCC fabrication by PAD. Particularly, the powder preparation workflow of ceramic particles is not transferable to most polymers. Mechanical powder preparation methods like ball milling, grinding, or cut milling, the typical processes used for ceramics, are associated with heating above the polymers' glass transition temperature and subsequent particle aggregation and/or particle shape changes. Therefore, the first aim of this work was to establish a polymer and PCC powder preparation routine for PAD. The key idea was to use polymer particles obtained by emulsion polymerization (with an average diameter below 1 μm and a narrow size distribution) in a "bottom up" approach, instead of ill-defined, aggregated particles from "top down" mechanical grinding processes. Polystyrene (PS) particles

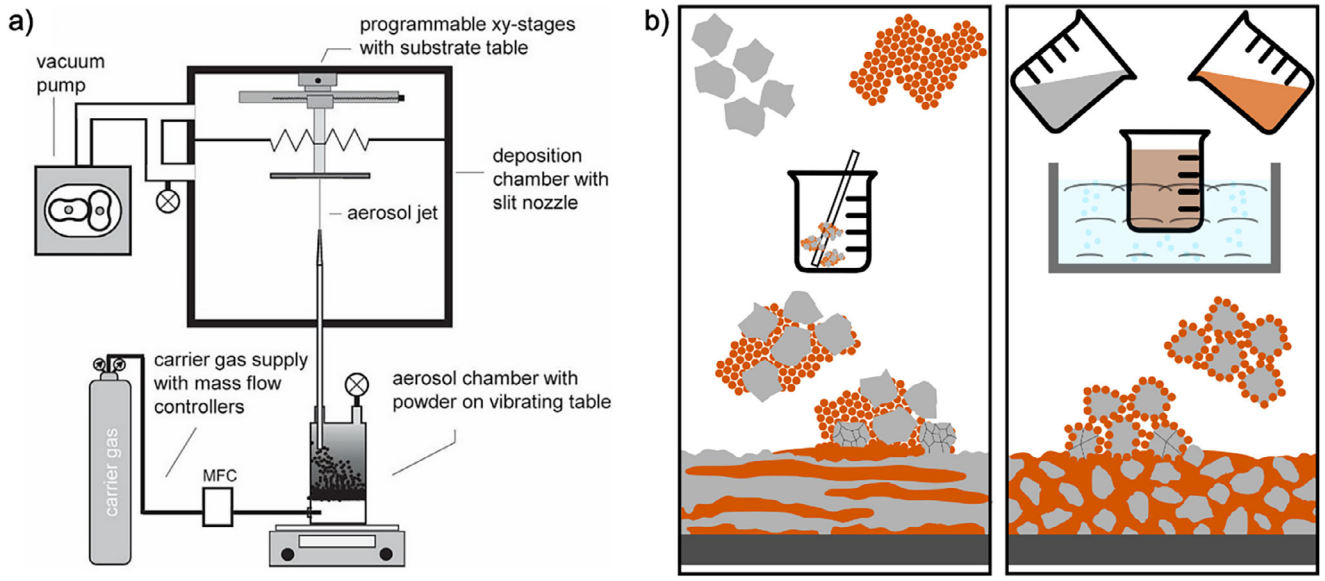

FIGURE 1 | (a) Schematic illustration of the PAD set-up consisting of an aerosol generation unit and a deposition chamber with the substrate. These are connected via a feedthrough that ends in a nozzle. The aerosolized particles are accelerated onto the substrate by a pressure difference between the two chambers using a carrier gas, and deposited on the substrate [24]. Reproduced with permission, Copyright 2015, The Authors, published by Göller Verlag GmbH. (b) Illustration of the different powder processing routines, and their impact on the resulting thin film microstructures. Left: Inhomogeneous PS/TiO_2 composite powder is prepared by hand-mixing, leading to separated PS-rich and TiO_2-rich areas in a multilayer-like film after PAD. Right: Homogeneous PS/TiO_2 composite powder is prepared as a slurry, ultrasonicated, and freeze-dried prior to PAD. During deposition, plastically deformed PS particles embed the partially fragmented or intact TiO_2 particles, forming an isotropic PCC thin film.

were used as a model system, which were then mixed with TiO_2 (rutile) particles and co-deposited on polycarbonate (PC) and steel. We established an ultrasound-based mixing method to obtain homogeneous composite powders from these components and could demonstrate that the morphology of the obtained PCC coatings could be tuned by the mixing conditions, as illustrated schematically in Figure 1b, so that either multilayer-like or homogeneous PCC films were obtained in a one-step process.

Second, our aim was to establish a PAD procedure that yields free-standing PS/TiO_2 thin films. This was so far not considered in the PAD community because PAD films typically have particularly good substrate adhesion. The free-standing films approach served two purposes: For one, the proof-of-concept for the fabrication of these materials by PAD should be highly interesting for the MEMS, sensors, and filtration materials communities. Also, and just as importantly, the availability of free-standing PAD-processed PCC films would greatly simplify the characterization of these materials, in particular their film composition. Such studies are currently often lacking in research on surface-attached PCCs, but are essential to investigate the effects of processing and precursor composition on the film properties. Our method to obtain flexible and robust free-standing PS/TiO_2 films by a sacrificial layer approach was inspired by our previous work on self-delaminating polymer films [69, 70], and the work by Khansur et al. [71]. These films enabled the quantitative determination of the actual film composition via thermogravimetric analysis (TGA), allowing for the identification of mismatches between the PCC powder and the film composition. This, in turn, can be used to understand the film formation mechanism. Lastly, we present a flexible 100 cm^2 PCC layer made from PS/TiO_2 deposited on a commercially available polyethylene terephthalate (PET) film as a demonstrator for potential membrane applications. Thus, the results presented below do not only give insights into the properties of the system PS/TiO_2 obtained by a robust, reliable PAD process, with potential applications as strongly adhesive UV protection layers, barrier coatings or flexible sensors, but the workflow can also be applied as a blueprint for the systematic powder preparation, fabrication and study of other PCC systems using PAD.

2 | Results

2.1 | Study Design

The aim of this study was to use PS particles obtained by emulsion polymerization for the fabrication of PS/TiO_2 PCC thin films in a robust, reproducible PAD process. As representative substrates, polycarbonate (PC) and stainless steel were used. We first investigated how the powder fabrication steps and the polymer concentration affected the homogeneity of the powders and the microstructure of the PCC films using scanning electron microscopy (SEM). Further, we investigated how the surface and cross-sectional morphology and thus the deposition mechanism of the PCC films differed from that of pure TiO_2. Using X-ray diffraction (XRD) and TGA, respectively, we obtained quantitative insights into the TiO_2 crystallite size and polymer content. By employing a mixture of poly(sodium 4-styrenesulfonate) (PSS) and glycerol as a sacrificial layer, a method to obtain free-standing PS/TiO_2 PCC films was developed. This was not only intended as proof-of-concept that free-standing films can be obtained by PAD, but also gave access to PCC thin film samples for analytical studies, especially for TGA. Finally, PET was chosen

as a commercially available model substrate to demonstrate larger-scale PS/TiO_2 PCC deposition for membrane applications.

2.2 | Powder Preparation

In light of the difficulties faced when attempting to obtain aggregate-free polymer powders in "top down" mechanical approaches, PS particles with a diameter of around 200 nm were synthesized "bottom up" by emulsion polymerization, a process which is known to yield particles with well-defined average size and size distribution. Details of the synthesis process are given in the Experimental Section, and the analytical data of the thus obtained PS particles are given in the Figure S1. In short, the two batches of particles had a mean particle size of 207 and 208 nm, respectively, and a dispersity of 0.056 and 0.015. TiO_2 particles were obtained using a classical PAD powder preparation routine involving sieving and drying as described in the Experimental Section. The characterization data (Figure S1) showed an average TiO_2 primary particle size of about 1 µm, forming small aggregates with an average diameter of about 3 µm.

The next crucial step was homogeneous mixing of the PS and TiO_2 particles. The polymer particles obtained by the surfactant-assisted emulsion polymerization process were electrostatically stabilized and thus did not aggregate while they remained in emulsion. However, once dried, they formed large, flake-like aggregates containing close-packed particles (Figure S1). Thus, it was critical to mix the PS and TiO_2 particles directly in the emulsion/slurry state, followed by sonication and freeze-drying to obtain a homogeneous powder (where homogeneous refers to the distribution of polystyrene and TiO_2 primary particles in the powder after freeze-drying). We also reversed the order of these steps to demonstrate the impact of powder preparation on the PAD layer morphology. We obtained an inhomogeneous distribution of primary particles consisting of TiO_2 clusters and freeze-dried PS flakes by manual mixing of the two components as solids. (Inhomogeneous refers to the particle level, while the distribution of the flakes and clusters within the overall powder is quite homogeneous, Figure 1b.) For each of these powder types, a variant with either 4 or 10 wt.% PS was prepared and used in PAD experiments alongside pure TiO_2 powder as a reference system.

The SEM images shown in Figure 2 illustrate the morphology and, to some extent, the internal structure of the homogeneous and inhomogeneous composite powders with 10 wt.% (a–d) and 4 wt.% PS (e–h). The color coding introduced in Figure 2 is used consistently throughout this work to represent the corresponding analytical data for each powder type and the resulting materials. Figure 2 indicates that in all cases, the powders consisted of aggregates larger than 10 µm. The overall structure of these aggregates differed markedly between the inhomogeneous and homogeneous powders (Figure 2a,c,e,g). At higher magnification (Figure 2b,d,f,h), further insights into the internal structure of these aggregates can be obtained. For the inhomogeneous 10 wt.% powder (Figure 2b), a distinct separation between the PS and TiO_2 components was observed. The PS domains consisted of flake-like, close-packed assemblies of primary particles that were surrounded by clusters of TiO_2 particles. These appear to be predominantly attached to the outer surfaces of the PS flakes. The aggregates found in the 4 wt.% inhomogeneous powder (Figure 2f) were similar. While a quantitative comparison between these two variants based on SEM images is not possible (as these do not provide sufficient statistically reliable information), what SEM clearly shows is the morphological contrast to the homogeneous powders. These have a regular distribution of finely dispersed PS and TiO_2 primary particles within the aggregates (Figure 2d for 10 wt.% PS, and Figure 2h for 4 wt.%, respectively).

The aggregates themselves (Figure 2c,g, respectively) appear elongated. This shape may originate from the freeze-drying process, possibly from the anisotropic, lamellar growth of ice crystals during freezing. While the overall morphology of the homogeneous powder aggregates appears comparable, their internal structure seems to differ slightly: aggregates in the 10 wt.% PS powder (Figure 2d) appears to be more densely interspersed with PS particles than those in the 4 wt.% PS powder (Figure 2h). While the homogeneous powders almost exclusively contain the types of aggregates shown in Figure 2, the inhomogeneous powders feature additional aggregate morphologies as illustrated in Figure S2. Besides TiO_2-rich (Figure S2a,b) and PS-rich aggregates (Figure S2e,f), aggregates composed solely of TiO_2 particles could be found (Figure S2c,d,g,h). Overall, the SEM images demonstrate that the powder preparation routine has a significant impact on the polymer-ceramic aggregate morphology, which will affect the subsequent PAD process.

2.3 | Surface and Cross-Sectional Microstructure of PAD Films on Different Substrates

The above-described inhomogeneous and homogeneous composite powders with 4 and 10 wt.% PS, respectively, as well as the pure TiO_2 powder, were each deposited on PC as a representative soft substrate, and on stainless steel as a representative hard substrate. For each material combination, the deposition was performed with an optimized parameter set as described in the Experimental section. Both the surfaces and the cross-sections of the thus obtained PAD films were imaged by SEM (Figures 3 and 4, respectively). Figure 3 displays SEM images of the PAD film surfaces deposited on PC (top row) and steel (bottom row). These show that the surface morphology of the PCC films, and thus potentially the film formation mechanism, is substantially different from that of the pure TiO_2 films (left column). The PCC films have comparably homogeneous and continuous surface morphologies on both substrate types, with no visible signs of chipping or delamination (middle column: inhomogeneous PCC, right column: homogeneous PCC). The surface morphology of the pure TiO_2 film on PC is also quite homogeneous, whereas large areas of chipping and detachment are evident on steel. A closer look at the composite films made from the homogeneous powder reveals somewhat fine-grained, uniform surface features, while the features of the films derived from the inhomogeneous powder appear more wave-like and non-uniform. The surface morphology of the pure TiO_2 films on PC is substantially finer than that of the homogeneous composite. We assume that the differently developed surface features may result from variations in the deposition mechanism and/or differences in the morphology of the impacting aggregates. The more irregular morphology of the pure TiO_2 films on steel may be attributed to the higher impact pressures that occur when depositing pure ceramic particles

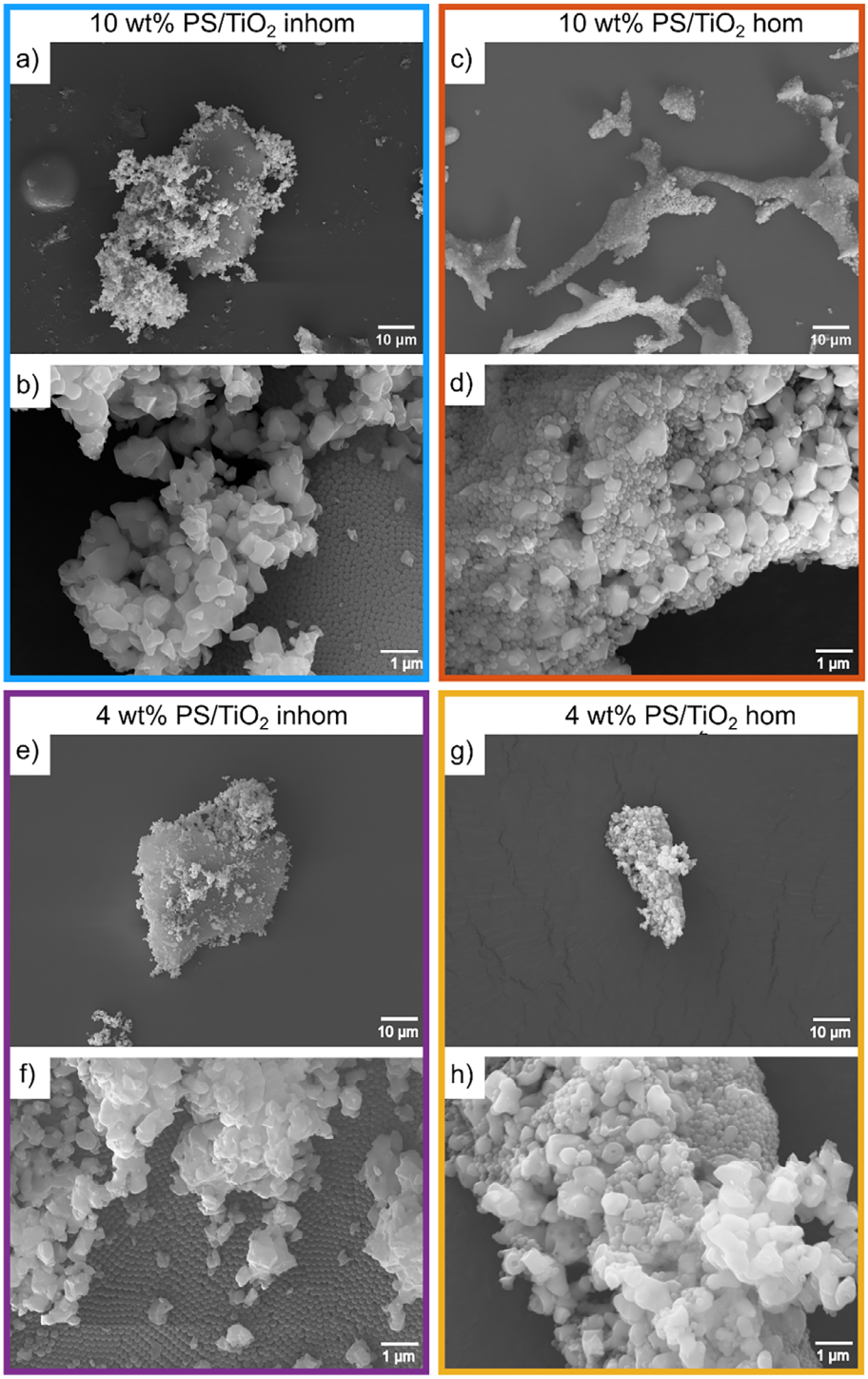

FIGURE 2 | SEM images of composite aggregates in the inhomogeneous (a, b, e, f) and the homogeneous PS/TiO_2 composite powders (c, d, g, h) with 4 (e, f, g, h) and 10 wt.% PS (a, b, c, d), respectively. In the inhomogeneous powder, PS primary particles form large flakes surrounded by TiO_2 particle aggregates (a, b, e, f). The homogeneous powder exhibits a more uniform distribution of PS and TiO_2 primary particles within each aggregate (c, d, g, h).

(no shock absorption effect), and to increased fragmentation and abrasion. The differences in surface morphology between the inhomogeneous and homogeneous composites, which are independent of the underlying substrate, can be qualitatively related to the different morphologies of the respective aggregates. However, the SEM images do not allow a more quantitative, statistically sound correlation.

The surface roughness parameter S_q (root mean square roughness) was determined for all films and the underlying substrates using laser scanning microscopy (LSM). Height maps recorded for a complete scan across the film (substrate – film – substrate) and the corresponding mean height profiles are shown in Figures S3 and S4, respectively. The data thus obtained (Table 1) show that in all cases, the film roughness was higher than the substrate

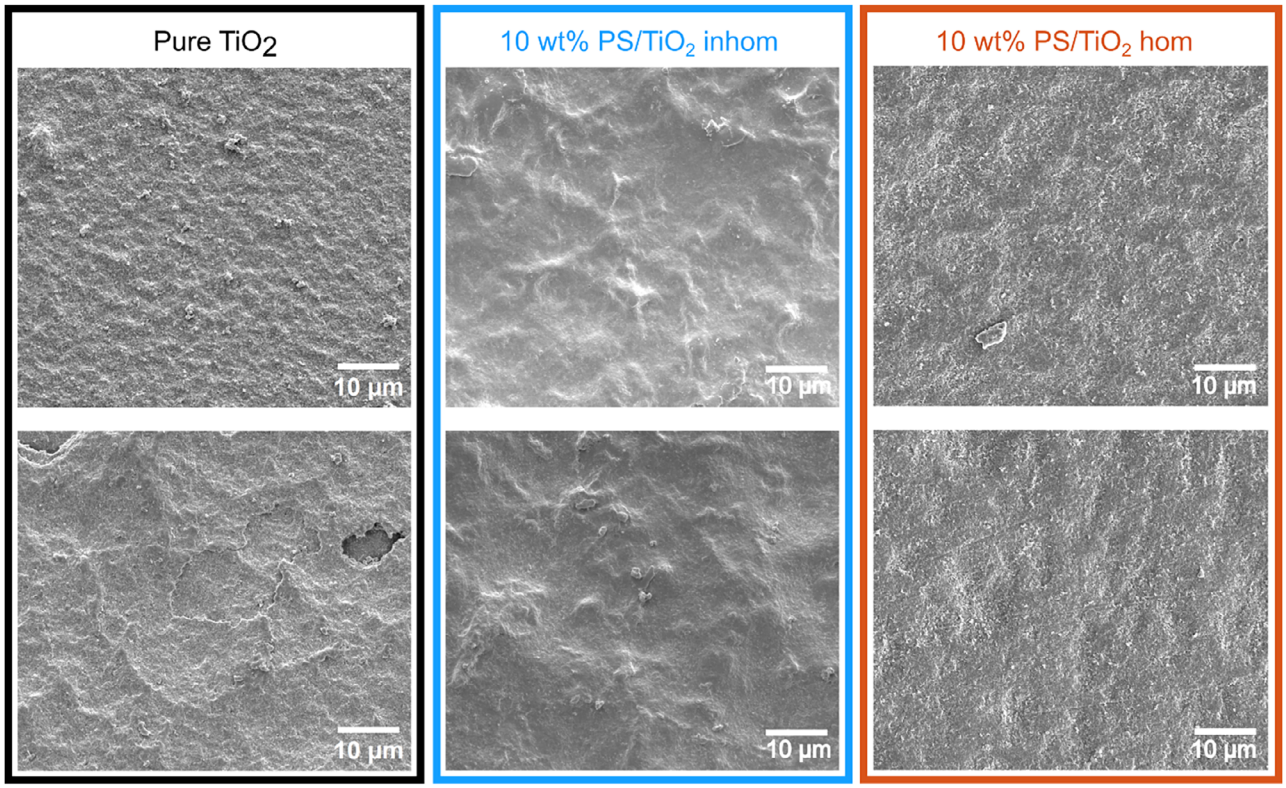

FIGURE 3 | SEM images of PAD film surfaces deposited on PC (top row) and stainless steel substrates (bottom row). From left to right, the columns show films made from pure TiO_2 powder, the inhomogeneous 10 wt.% PS/TiO_2 powder, and the homogeneous 10 wt.% PS/TiO_2 powder. The surface morphology of all composite films is similar and shows no signs of chipping. In contrast, the pure TiO_2 film exhibits substrate-dependent features, with smooth coverage on PC and large chipped areas on steel.

TABLE 1 | Root-mean-square surface roughness S_q for the surfaces shown in Figure 3 ($S_{q,film}$), together with the S_q of the corresponding substrates ($S_{q,sub}$). Statistical uncertainty intervals are given for substrate values (three measurements on the same substrate type); no calculated statistical uncertainty intervals are given for the single film measurements.

Substrate material	$S_{q,sub}$ / $S_{q,film}$ (µm) TiO_2	$S_{q,sub}$ / $S_{q,film}$ (µm) Inhomogeneous PS/TiO_2	$S_{q,sub}$ / $S_{q,film}$ (µm) Homogeneous PS/TiO_2
PC	0.16 ± 0.06 / 0.47	0.19 ± 0.06 / 1.74	0.05 ± 0.06 / 0.72
Steel	0.41 ± 0.01 / 1.56	0.43 ± 0.01 / 1.40	0.41 ± 0.01 / 0.64

roughness. The PCC films obtained from homogeneous powder consistently had a much lower roughness value than the films obtained from the inhomogeneous ones. This observation is in good agreement with the SEM images.

Cross-sections of the PAD films were prepared using a focused ion beam (FIB) as described in the Experimental section, and imaged using SEM (Figure 4). In these images, PC substrates appear darker than the stainless steel substrates. A bright platinum-based, beam-induced coating is visible above the films, which was applied with the FIB to protect the region of interest. The pure TiO_2 films (Figure 4, left column) had a compact microstructure containing numerous defects, including cracks and voids on both substrates. On steel, horizontal cracks extended across large areas of the film, also parallel to the film-substrate interface. The voids of the film on PC seemed more localized. The boundaries of primary TiO_2 particles were no longer discernible within these films, except at the interface with the PC substrate. Surprisingly, the composite films made from the inhomogeneous PS/TiO_2 powder (middle column, termed "inhomogeneous films" from now on) exhibited a multilayer-like structure with a fairly regular spacing, with large PS clusters (dark) separated by layers of TiO_2 particles (bright). Cracks were again observed on the steel substrate, particularly at the film-substrate interface, but not in the inhomogeneous composite film deposited on PC. The TiO_2 phase in these films apparently consisted of fragments of the original particles, suggesting substantial particle break-up during substrate collision. The films made from the homogeneous composite powder (Figure 4, right column, termed "homogeneous films" from now on) displayed a distinctly different, isotropic microstructure, with a continuous polymer phase embedding the ceramic particles, as expected for a polymer matrix composite. The TiO_2 particles appeared less fragmented than in the inhomogeneous composite film, with clearly discernible larger fragments

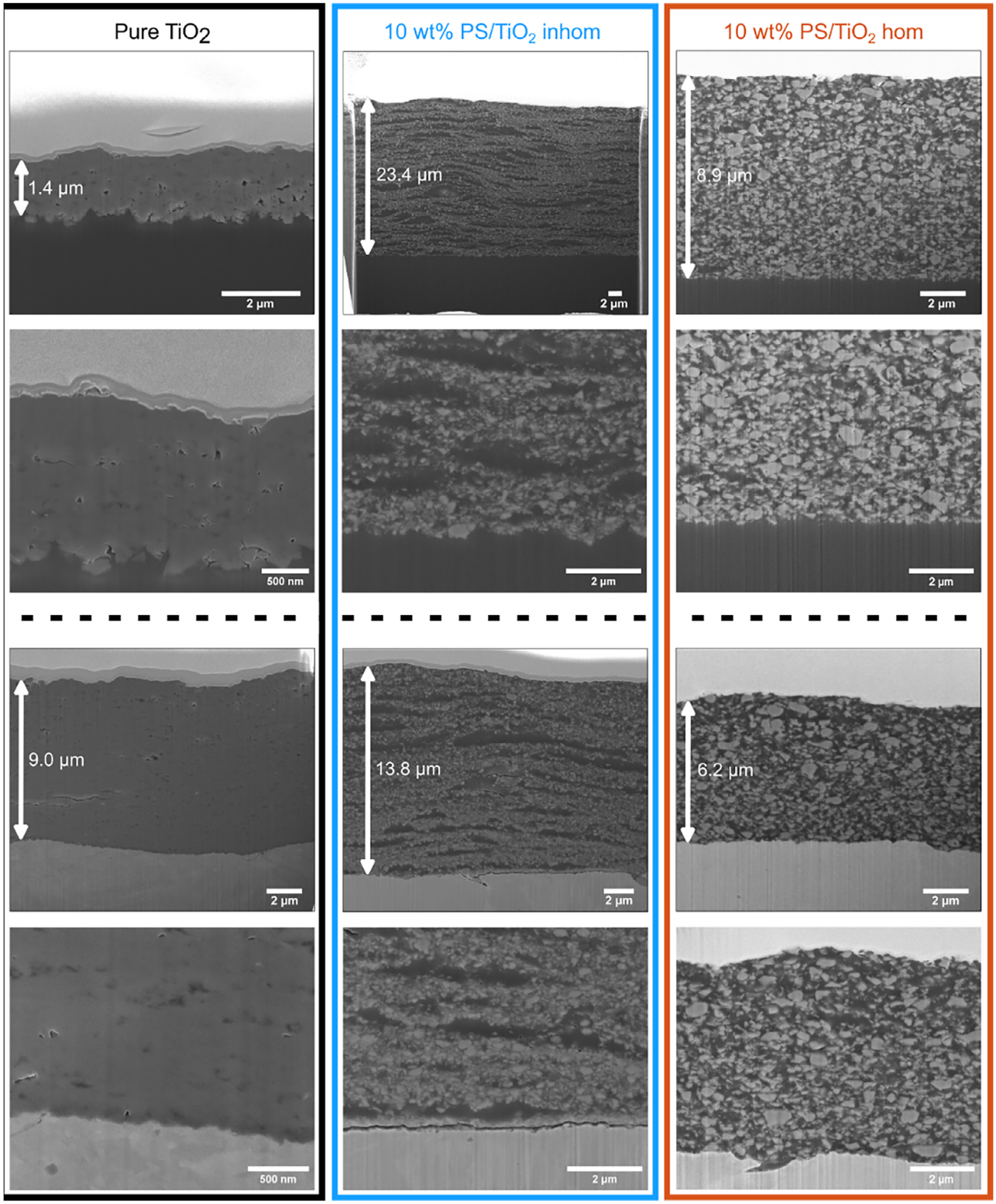

FIGURE 4 | Cross-sections of PAD films deposited on PC (top) and stainless steel substrates (bottom) prepared by FIB and imaged by SEM: Pure TiO_2 (black), inhomogeneous 10 wt.% PS/TiO_2 PCC (blue), and homogeneous 10 wt.% PS/TiO_2 PCC (orange). For each substrate, an overview of the cross-section showing the overall film thickness and a corresponding zoom-in of the film-substrate interface are shown (stacked vertically). The pure TiO_2 films exhibit a compact, defect-rich morphology, with embedded TiO_2 particles visible at the PC interface. Films derived from the inhomogeneous composite show a multilayer-like structure with alternating PS-rich and TiO_2-rich regions, and cracks at the steel interface. The homogeneous composite films resemble a polymer matrix composite with homogeneously distributed TiO_2 and plastically deformed PS filling substrate defects, contributing to good mechanical anchoring on both substrates.

and even intact primary particles. No defects were evident within these cross-sections.

The thickness of the 10 wt.% inhomogeneous composite films was significantly higher than that of pure TiO_2 films when deposited using identical process parameters (gas flow: 3 standard liters per minute (slm) / 10 scans at a scan rate of 1 mm s^{-1}), especially on PC (23.4 µm for composite vs. 1.4 µm for pure TiO_2). On steel, the same trend was observed (13.8 µm for the composite vs. 9.0 µm for pure TiO_2).

The homogeneous 10 wt.% PS/TiO_2 composite films, which were deposited using a different optimized parameter set (6 slm / 25 scans at 5 mm s^{-1}) had a lower thickness (8.9 µm for the composite on PC, 6.2 µm for the composite on steel). However, this is most likely not due to differences in the parameter set: For example, a stronger fragmentation was observed in the inhomogeneous film at a gas flow rate of 3 slm, compared to 6 slm for the homogeneous one. Yet at the higher particle velocity and impact pressure, more fragmentation would be expected for the homogeneous film, and not vice versa. Thus, the observed differences should originate from the different powder morphologies.

Besides studying the overall film morphology, it is instructive to investigate the film-substrate interface in more detail for conclusions about the film deposition mechanism. All three film types had good adhesion to the PC substrates, with no cracks and voids along the interface (zoomed images in Figure 4). Embedded TiO_2 particles within PC were visible for the pure TiO_2 film, which also had a rugged interfacial morphology. The interface of the two composite films with the substrate was relatively smooth. This indicates that some kind of anchor layer formed during PAD of TiO_2 on PC, with substantial interfacial deformation of the substrate. This was more pronounced for TiO_2 on PC than for TiO_2 on steel, where no ceramic penetrated into the substrate due to the higher stiffness of steel. The interface of the homogeneous PCCs showed no signs of particles inserted into the substrate. Plastically deformed PS was found within a steel surface defect, illustrating the excellent ability of these coatings to conform to the substrate morphology without damage. Interestingly, the inhomogeneous PCC film on steel had marked delamination cracks at the interface, while it had good adhesion to the PC substrate.

Taken together, the differences observed in both the surface and the cross-sectional SEM images suggest a substantial effect of the powder and substrate type on the film morphology. This points toward a different deposition mechanism for pure TiO_2 compared to that of the PCC powders, especially since no anchor layer was observed in the case of the PCCs.

2.4 | XRD Measurements of PAD Films on Polycarbonate Substrates

Pronounced fragmentation of the ceramic particles was observed in the SEM images of the inhomogeneous PCC films. To confirm and quantify this observation, XRD measurements were performed both on the films (pure TiO_2 and both types of PCC coatings on PC substrates) and on the initial TiO_2 powder before deposition (Figure 5a). The data were refined using the Rietveld method. The Rietveld refinement data for all samples shown in Figure 5 are provided in Figure S5. Due to correlations between strain and crystallite size, only the latter was used for the Rietveld refinements, leading to the presented trends. All intensities were normalized to the maximum of the (110) reflection and then shifted vertically to facilitate comparison. A magnified view of the (110) reflection is presented in Figure 5b to visualize the peak broadening. While the TiO_2 powder had one sharp peak (the second peak is unfiltered $K_{\alpha,2}$ radiation) corresponding to 145 nm crystallites, the pure TiO_2 coating exhibited a broad peak corresponding to a reduction of the crystallite size to 16 nm, indicating strong TiO_2 fragmentation in the absence of polystyrene. Slightly narrower peaks corresponding to crystallites of 21 nm average diameter were observed for both the 10 and 4 wt.% inhomogeneous coatings. The crystallites of the homogeneous ceramic PS/TiO_2 coatings were significantly larger (50 nm for 10 wt.%, 27 nm for 4 wt.%). This is in line with the observed trend of less fragmentation in the homogeneous films observed by SEM. It demonstrates that the extent of shock absorption by the polymer powder depends on the homogeneity of that powder, and that such shock absorption can more substantially reduce fragmentation than solely shock absorption by the substrate.

In addition to the crystallite reflections in Figure 5a, the diffractograms of all the PAD film samples exhibit an amorphous halo from about $2\theta = 15°–25°$. The exact shape and range vary without a clear trend. These halos originate from the PC substrate and, in the case of the composite films, from the deposited PS. Since the individual amorphous polymer contributions cannot be separated, no further interpretation is possible at this point.

2.5 | Compositional Analysis of PAD Films via a Sacrificial Layer Approach and TGA

Since the crystallite size reduction observed in the coatings appears to correlate with the polymer content and its distribution within the composite powders, it is important to verify whether the polymer content in the deposited films reflects that of each of the feedstock powders used. During PAD, losses or redistribution of the polymer component cannot be excluded, particularly when considering the different deposition efficiencies (reflected by the film thickness) and film morphologies observed for the homogeneous and inhomogeneous composites. Determining the composition of PAD films is challenging, as commonly used spectroscopic methods such as attenuated total reflection Fourier-transform infrared spectroscopy or energy-dispersive X-ray spectroscopy provide only qualitative or surface-localized information. To obtain quantitative compositional data, a method to remove the film from the substrate was developed to make it accessible for thermogravimetric analysis (TGA). This was achieved by applying a sacrificial, water-soluble polymer layer between the substrate and the PAD film. This allowed floating the film off the substrate by immersion into water, and thus, after thorough drying, a quantitative comparison of the PCC film and powder composition by TGA. Since we demonstrated above that the substrate properties did not critically affect the film properties, it is justified to assume that the same is true for the thin sacrificial layer. Each TGA sample consisted of six PCC films made in three different PAD runs. This provided enough material both for the experiment and a sound statistical average.

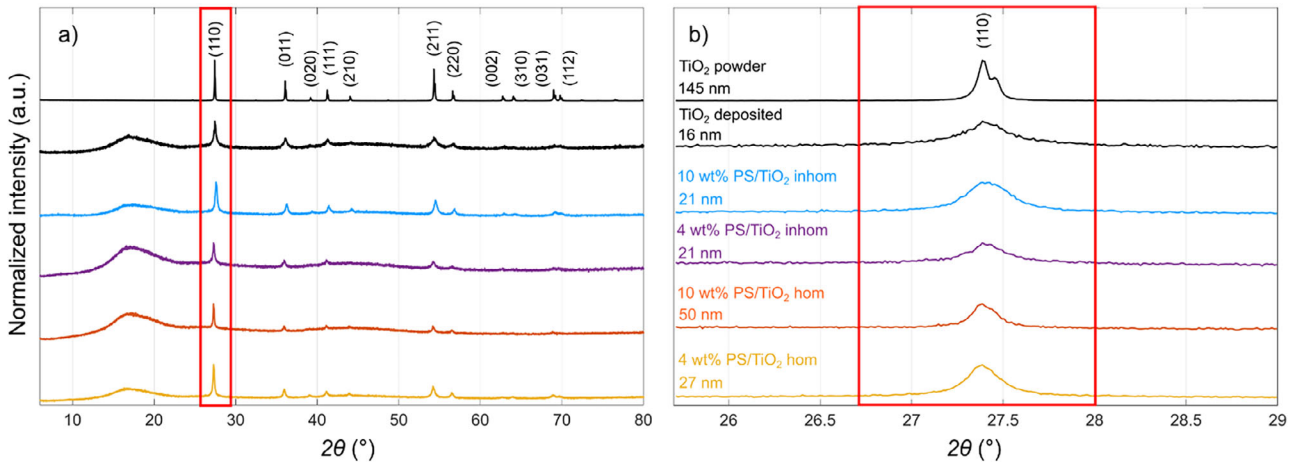

FIGURE 5 | XRD diffractograms of the TiO2 powder before PAD, the pure TiO2 film on PC, and the four different PS/TiO2 composite powders deposited on PC substrates. (a) Overview, (b) zoom-in of the (110) reflection of TiO2. Sample labels and the calculated crystallite sizes are included in (b). Intensities were normalized to the highest (110) peak of each sample. Shape changes in the (110) reflection are observed. Peak broadening indicates reduced crystallite sizes, most pronounced for the pure TiO2 film, slightly less for the inhomogeneous and 4 wt.% homogeneous composites, and least for the 10 wt.% homogeneous composite. This reflects differences in the shock absorption due to PS content and distribution.

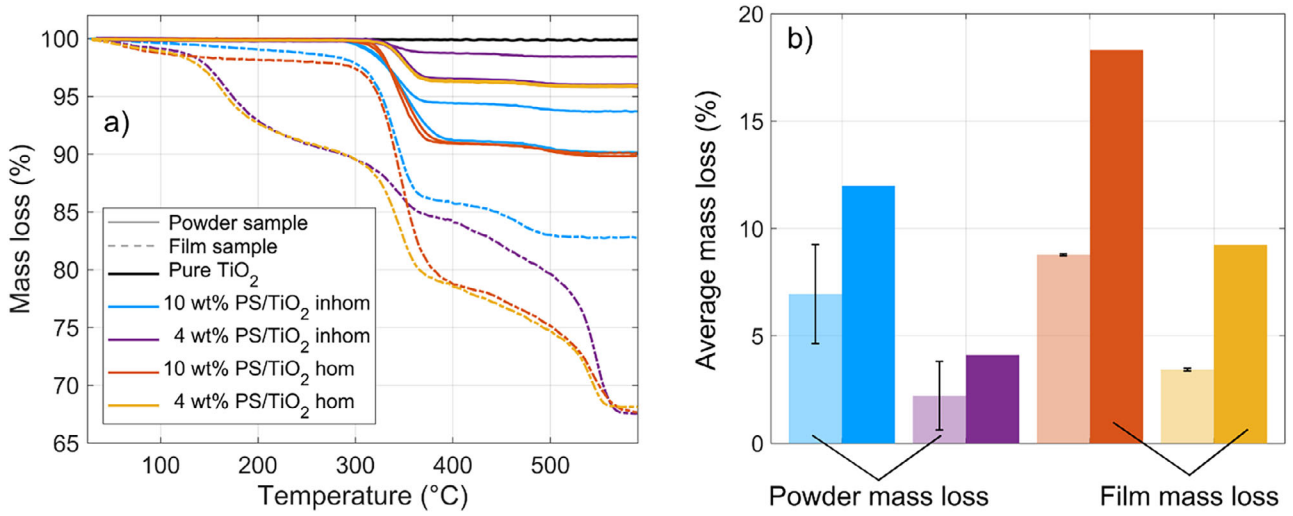

FIGURE 6 | (a) TGA curves of PS/TiO_2 powders (solid lines) and corresponding films (dashed lines) show a higher polymer content in the films than in the powders, as well as multistep thermal degradation of the films. (b) Grouped bar plot of average mass loss for each sample type (left, semi-transparent bar = powder; right, solid bar = PAD film), revealing compositional variations between homogeneous and inhomogeneous powders and films. The PCC films consistently had a higher PS content than the powders. The color code in (b) is the same as in (a).

The samples were heated in the presence of oxygen to burn the organic component and determine the corresponding mass loss. In Figure 6a, the TGA curves of the PS/TiO_2 composite powders (solid lines), the corresponding PCC films (dashed lines), and pure TiO_2 powder as a reference (black solid line) are shown. While the pure TiO_2 powder expectedly shows no remarkable mass loss over the whole temperature range, the composite samples exhibited various mass loss events reflecting sequential sample decomposition at different temperatures. The powders featured a two-step degradation process with a pronounced mass loss around 300°C and a minor secondary loss near 460°C. It is well established in the literature that pure, additive-free PS undergoes thermal degradation in an oxidative atmosphere, with one major mass loss occurring between 300–400°C. The degradation behavior of the pure PS powders shown in Figure S6 is consistent with these literature reports, as is the major mass loss of all composite powders. The second mass loss at higher temperatures can be associated with the surfactant content of the PS particles, a result of their origin from emulsion polymerization. Two TGA traces are shown for each powder. While the traces of both homogeneous powders are concurring, those of the inhomogeneous powders differ strongly, indicating that the composition of the hand-mixed powders varied – possibly due to the difficulty of homogenizing the large, light PS flakes with the dense TiO_2 clusters in the solid state.

The films displayed a three-step decomposition process. An initial mass loss (from ~120°C to ~300°C) was observed for all four PCC films, but was less pronounced for the 10 wt.% composite films than for the 4 wt.% one. The second mass loss, which was the

major mass loss for all PCC films except the inhomogeneous 4 wt.% inhomogeneous one, started at around 300°C, and a third mass loss was observed above 400°C, which markedly varied in magnitude between the different samples. After that, the TGA curves of all PCC samples except the 10% PS/inhomogeneous one converged to the same baseline at ~ 67% mass loss, while the 10% PS/inhomogeneous film remained at ~ 83%.

Early mass losses are typically attributed to the evaporation of residual moisture in polystyrene and/or the desorption of –OH groups bound to TiO_2 particle surfaces. The small amount of initial mass loss of both 10% PS samples is consistent with this explanation. However, the origin of the large initial mass loss of both the homogeneous and the inhomogeneous 4 wt.% film samples remains unclear. Artifacts from the film preparation are unlikely since all four PCC films underwent the same treatment. The second mass loss of all PCC films can be assigned to polystyrene degradation. The mass loss in the third step indicates additional contributions besides polystyrene. This could include residual PSS (decomposition temperature range of PSS sodium salt: 420°C–510°C) from the sacrificial layer that may not have been fully removed after film release, possibly due to the strong particle-PSS film interactions during impact, or even chemical bond formation. The amount of PSS thus bound could vary, which explains the lack of a trend for this thermal process in the four PCC films.

For a comparative analysis, the degradation temperature and mass loss of the second step of the films (assigned to polystyrene) were analyzed. The evaluation was conducted using the tangent method described in DIN EN ISO 11358 [74]. The degradation temperature was determined as the onset temperature of the degradation step. The TGA and dTGA curves of the 10 wt.% inhomogeneous film sample evaluated according to this procedure are shown as an example in Figure S7. The degradation temperatures determined vary only slightly between the powder and film samples and cluster around an average value of 322 ± 10°C. This value is slightly lower than the degradation temperature of the pure PS powder batches (349°C, Figure S7). The mass losses associated with this degradation process differ substantially. For clarity, Figure 6b summarizes the average mass losses in a grouped bar diagram, with the semi-transparent bars representing the powders and solid bars representing the films.

The data show that the homogeneous powders already had a lower mass loss than expected based on their nominal PS content. This indicates a limited accuracy of the method for these samples in the range of 1%–2%, thus data variation in this range should not be overinterpreted. The mass loss of the inhomogeneous powders appears even lower due to the above explained strong data scattering. Importantly, all films had a higher polystyrene content than their respective powders. The effect is seen most strongly in the homogeneous films, with roughly 9 and 18 wt.% polymer content – about twice as much polymer as was present in the respective starting powders. These results indicate that the polymer is deposited preferentially in the homogeneous case, i.e., aggregates with higher local polymer content seem to be aerosolized and incorporated more easily, possibly due to their lower density. As shown by SEM, the two inhomogeneous PCC powders contain highly variable aggregate structures, including pure TiO_2 aggregates. This counteracts a preferential polymer incorporation.

2.6 | Analysis of the PAD Process Characteristics

To better understand how the powder characteristics translate into film formation, it is instructive to examine the underlying PAD process behavior. For this purpose, we analyzed the powder discharge rates, deposition rates, and deposition efficiencies of the PAD deposition of all composite powders, with pure TiO_2 as a reference. The results are presented in Figure 7. The discharge rates obtained for the different powders are summarized in Figure 7a. The 4 wt.% inhomogeneous PCC powder had a discharge rate similar to that of pure TiO_2, the other powders had, within the limits of statistical significance, higher and about equal discharge rates. Thus, both a higher polymer content and a more homogeneous distribution led to higher powder discharge.

As Figure 7b shows, the powder discharge rate data scatters strongly – a known phenomenon for co-deposition of mixed-density feedstocks, which should not be overinterpreted. Apparently, there is a general tendency toward faster deposition with increasing polymer content. The deposition efficiency, which is calculated from the powder discharge rate and the deposited mass, seems lower for all PCCs than for pure TiO_2, although the data also strongly scatters (Figure 7c). The two homogeneous PCCs had the same discharge rate and deposition efficiency, maybe because the aggregate type found in these powders is homogeneous and similar between the samples. A pronounced substrate effect is observed for all PCCs but not for TiO_2, with consistently higher deposition efficiency on PC than on stainless steel. This indicates that shock absorption through the powder and the substrate influences the deposition efficiency both individually and in combination. Definitive assessment of the influence of each – or even a comparison of the contribution of shock absorption by the powder type – is challenging and will require further study. Insight could potentially be gained from simulation studies that attempt to capture the extent of the deformation zones within the film cross-section during the impact of individual particles or aggregates.

Shock absorption is not necessarily favorable. It seems to reduce the deposition efficiency of the process in general, as seen in the values obtained for pure TiO_2 that exceed those of the composites, especially on steel. Overall, our process-related data confirms the notion that polymer-containing powders deposit by a substantially different PAD mechanism than pure ceramics on (mostly) hard substrates [52, 55, 57, 65–67]. If we interpret the deposition efficiency as an indicator of such a change in deposition mechanism, we can assume that this mechanism may remain essentially identical for the two homogeneous composites, consistent with the assumption that aggregates of similar outer shape and inner structure dominate deposition in both cases.

In summary, when correlating discharge rate, deposition rate, and deposition efficiency with microstructural and compositional findings, a coherent picture emerges. The inhomogeneous

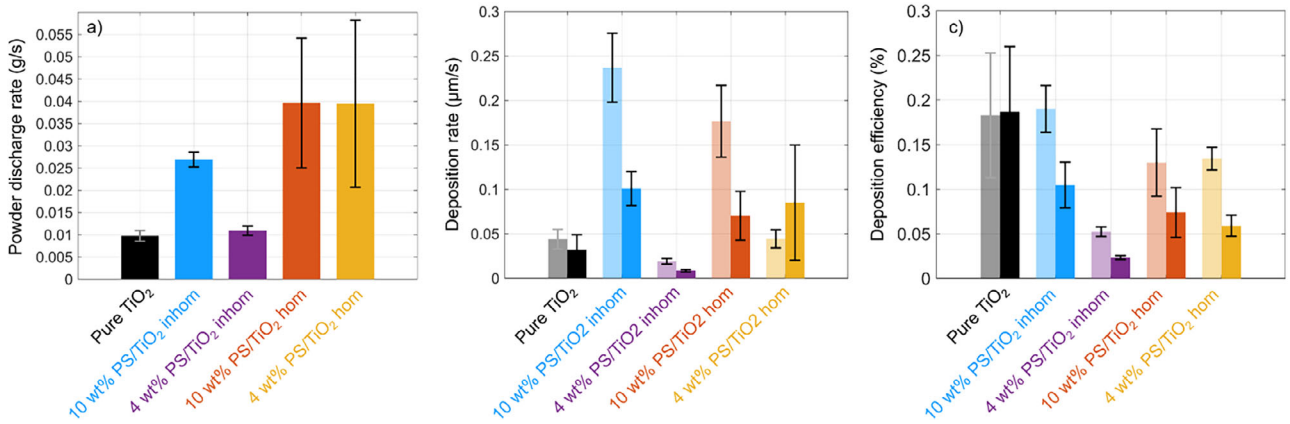

FIGURE 7 | (a) Powder discharge rate (in g s^{-1}) for the different powders at a carrier gas flow of 3 slm, showing considerable scatter for some powder types. (b) Deposition rate (µm s^{-1}) on PC (semi-transparent bars, left) and stainless steel (solid bars, right) grouped by powder type, revealing consistently higher rates on PC than on steel for all powders. (c) Deposition efficiency with the same grouping as in (b).

10 wt.% composite film has a TiO_2-rich composition (according to TGA, Figure 6) and a multilayer-like morphology (Figure 4). This morphology reflects the sequential stacking of the polymer-rich and TiO_2-rich composite powder aggregates. In contrast, the homogeneous composites, despite exhibiting the highest discharge rates, form smoother, isotropic films with higher polymer content and larger TiO_2 crystallites – the latter feature indicative of stronger shock absorption through the polymer powder. For these powders, the internal architecture of each aggregate – rather than the aggregate size – becomes the decisive factor controlling impact behavior and film formation. Their deposition rates are only moderately lower than that of pure TiO_2, suggesting that the more uniform aggregates still pack efficiently enough to yield comparable volumetric growth, albeit with reduced mass transfer compared to the TiO_2-rich inhomogeneous film.

2.7 | Proof-of-Concept Demonstrators for PCC Composite Films

Two demonstrators illustrate the functional potential of the PCC films (Figure 8). As a first demonstrator, the inhomogeneous 10 wt.% PS/TiO_2 powder was employed to uniformly coat a 10 cm × 10 cm PET film, yielding a composite layer that remained well adhered and mechanically stable even under pronounced bending (Figure 8a). Such robustness highlights the suitability of these films for flexible barrier or filtration applications. Despite this potential, it should be noted that the deposition efficiency of PAD is very low, typically well below 1%. A key requirement for any future technological implementation would therefore be either a substantial increase in this efficiency or an effective recycling strategy for the starting powders, ideally within a closed-loop process.

As a second demonstrator, the sacrificial layer approach enabled the preparation of free-standing PCC films that were several micrometers thick (Figure 8b). Notably, these membranes maintained structural integrity without a supporting substrate and displayed a high degree of flexibility. Composite films of this type, which could be attractive for flexible electronics, dielectric layers, barrier coatings, or filtration membranes, have not, to the best of our knowledge, been reported before in a sufficiently stable form to be manually handled and transferred. While PS/TiO_2 served as a model system in this study, the concept could readily be extended to more application-oriented compositions, for example, by replacing PS with conductive or antimicrobial polymers to create novel functional materials.

3 | Discussion

For PAD involving a polymeric component, a shock absorption effect has been proposed. This effect was originally described for ceramic coatings deposited on polymer substrates and is interpreted as part of the kinetic energy of the impacting particles being dissipated through deformation of the polymer substrate, in addition to fragmentation and plastic deformation of the ceramic particles [68]. As a result, the impact pressure of particles is reduced [68], and the conventional RTIC mechanism is only partially observed for these systems. In the following, we will refer to this effect as the external shock absorption effect. A similar shock absorption effect has been reported for the deposition of PCC powders. It is independent of the nature of the substrate and can be related to the plasticity of the polymer component of the deposited powder [32, 51–53, 55, 57, 59–61, 63, 65]. This will be referred to here as the internal shock absorption effect. In both cases, a larger crystallite size of the ceramic phase, determined by XRD, compared to systems without polymer content was observed [32, 51–53, 55, 57, 59–61, 63, 65, 68, 72]. Thus, the crystallite size is a reliable indicator of the amount of shock absorption occurring during the deposition process. Structural characteristics of the external shock absorption effect include partially fragmented ceramic particles embedded in the substrate surface, accompanied by insufficient film densification and defect-rich microstructures [61, 68, 72, 73]. Such features are observed for the pure TiO_2 films deposited on PC substrates (see Figure 3). In contrast, the internal shock absorption effect is associated with features such as an altered surface texture with increased roughness compared to purely ceramic systems [59, 62, 63, 65]. In the case of PS/TiO_2 on PC presented here, a

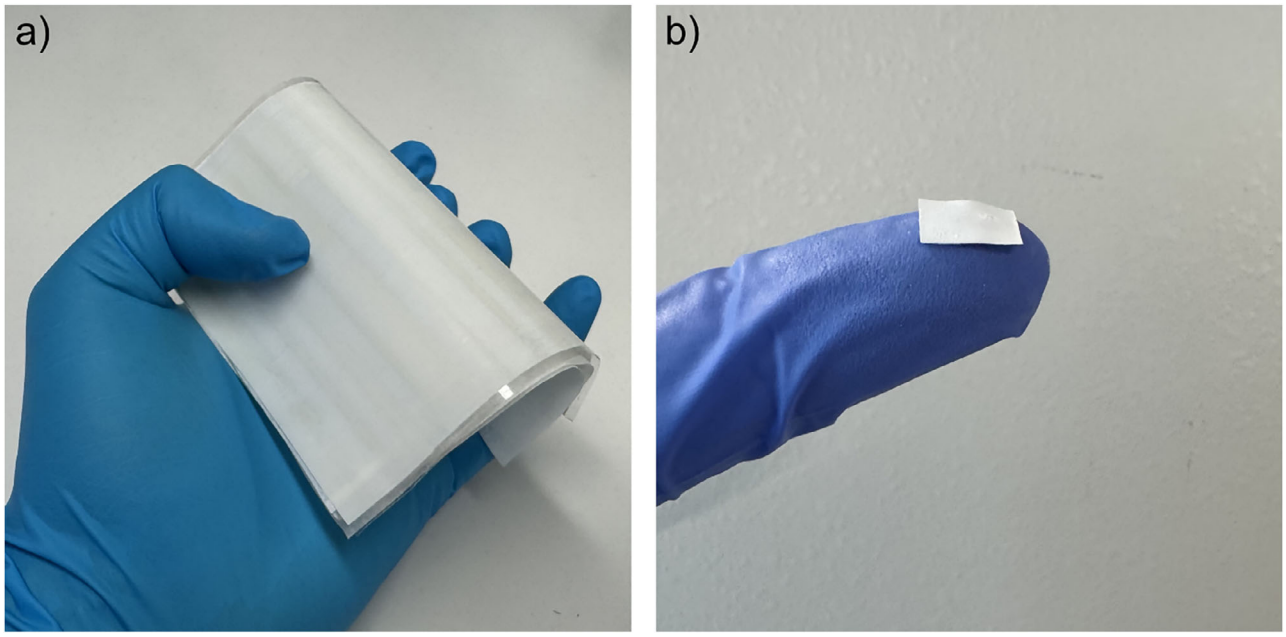

FIGURE 8 | (a) Composite film deposited from the 10 wt.% PS/TiO_2 inhomogeneous powder on a 50 μm thick PET film remains intact even when the substrate is bent. (b) Free-standing, thin film produced from the same powder via a sacrificial layer approach, demonstrating mechanical stability after release from the substrate.

slightly increased surface roughness compared to pure TiO_2 films was observed for homogeneous PS/TiO_2, and a substantial one for inhomogeneous PS/TiO_2 (Table 1). On steel, the roughness values for both PCCs are similar to those on PC, while that of pure TiO_2 is significantly higher than on PC. This indicates that the surface roughness is dominated by the powder properties and not the underlying substrate for both PCCs. As the homogeneous composite coatings had significantly smoother surfaces, the extent of surface roughness enhancement associated with the internal shock absorption effect seems to depend on the powder homogeneity. The homogeneous distribution appears to facilitate a more uniform dissipation of the kinetic energy into deformation energy during impact, thereby promoting smoother film formation. In contrast, the inhomogeneities within the composite powder may locally amplify deformation and particle rearrangement. For instance, regions may exist in which predominantly TiO_2 particles impact the surface, while in others, PS or composite aggregates arrive in greater numbers. As a result, inhomogeneities on the scale of the TiO_2 particle size (a few micrometers or less) may occur alongside larger inhomogeneities on the order of the composite aggregates (several tens of micrometers).

The cross-sectional images of Figure 4 also suggest that the internal shock absorption effect and not the external shock absorption effect is the dominant factor for PCC film formation. This is indicated by the finding that the underlying substrates do not seem to influence the microstructure of the composite coatings in a significant way. Thus, in summary, the PCC powder characteristics and not the properties of the underlying substrate dominate both the PCC film morphology and roughness—a factor that, to the best of our knowledge, has not been addressed in the literature so far. However, the data shows a substrate influence on the interfacial adhesion, at least for the inhomogeneous powders.

4 | Conclusion and Outlook

In summary, this study addressed the influence of powder morphology and polymer content on the powder aerosol deposition behavior of PS/TiO_2 composites using powders prepared by two distinct routes – homogeneous mixing in the emulsion state, and inhomogeneous blending after drying. By systematically comparing microstructure, crystallite size, and polymer content with the powder discharge rate, deposition rate, and deposition efficiency, a consistent picture emerges: the homogeneous composites form isotropic films with smooth surfaces and comparatively large crystallite sizes, indicative of pronounced internal shock absorption and uniform energy dissipation during impact. In contrast, the inhomogeneous composites display a multilayer-like morphology with localized polymer-ceramic segregation, lower crystallite sizes, and particularly high deposition rates and efficiencies in the 10 wt.% case, suggesting that localized TiO_2-rich domains dominate film growth. The pure TiO_2 films follow the classical RTIC mechanism, even though external shock-absorption occurs on PC, with partly dense, defect-rich microstructures. Overall, the data implies that the deposition mechanism of the homogeneous composites is governed by uniformly mixed aggregates, for which a consistent stoichiometry is assumed, whereas the inhomogeneous composites deposit via structurally heterogeneous aggregates in which TiO_2-rich parts of the aggregates preferentially contribute to film formation. These findings highlight that not only the polymer fraction but also its spatial distribution within the powder critically determines the balance between internal and external shock absorption and thereby controls both film structure and deposition efficiency.

In addition to the potential application examples discussed in this work – such as the use of the system as a membrane material – it must again be emphasized that the low deposition efficiency of PAD currently limits its applicability. In this context, future work

should focus on developing recycling strategies for the starting powder and further improving the deposition efficiency.

5 | Experimental Section

5.1 | Materials for the Preparation of PS Nanoparticles

Styrene (S, 99%) was purchased from Fisher Scientific GmbH (Schwerte, Germany). Butanediol diacrylate (BDDA, technical grade), sodium dodecyl sulfate (SDS, ≥98,5%), sodium persulfate (NaPS, ≥98%), sodium disulfite (NaDS, for analysis) and potassium hydroxide flakes (KOH, 90% reagent grade) were purchased from Sigma–Aldrich (Darmstadt, Germany). The anionic surfactant Dowfax 2A1 was purchased from EZkem (Hood River, OR, United States). Radical inhibitors were removed from the monomers before emulsion polymerization by passing them through a basic alumina column (50–200 µm, Acros Organics, Schwerte, Germany).

5.2 | Materials for PAD

Titanium dioxide powder, rutile (≥98%), metals basis with a primary particle size of 0.9–1.6 µm as specified by the supplier, was purchased from Fisher Scientific GmbH (Schwerte, Germany). Polycarbonate (PC, Lexan 8010 MC, 500 µm) substrates were purchased from König Folienzentrum (Wuppertal, Germany). Stainless steel substrates (AISI 316L, 1 mm) were purchased from RCT Reichelt Chemietechnik GmbH + Co (Heidelberg, Germany). Poly(ethylene terephthalate) film (Hostaphan RNK 50, 50 µm) was purchased from Mitsubishi Polyester Film GmbH (Wiesbaden, Germany). Poly (sodium 4-styrenesulfonate) (PSS, weight average molar mass ~ 70.000 g mol^{-1}) was purchased from Sigma–Aldrich (Merck KGaA, Darmstadt, Germany). Glycerol (≥ 98.5%) was purchased from Th. Geyer GmbH & Co. KG (Renningen, Germany).

5.3 | Synthesis of PS Nanoparticles

Synthesis of polystyrene particles was performed in a 1 L double-walled reactor equipped with a stirrer (IKA Ministar 20 digital, IKA mbH, Staufen, Germany) and a reflux condenser under a nitrogen atmosphere at 85°C. To remove oxygen from the deionized water used in synthesis, it was degassed with nitrogen for 30 min. Two batches of polystyrene particles were synthesized using the same recipe. For the first batch (PS01), the reactor was filled with a monomer emulsion (ME1) consisting of 6.75 g styrene, 0.761 g BDDA, 0.391 g SDS, and 527 g deionized water. While the emulsion was stirred at 225 rpm, the polymerization was initiated by adding 0.959 g NaPS and 0.138 g NaDS. After 15 min, a second monomer emulsion (ME2) was added by a rotary piston pump (Ismatec ISM321A – RH0CTC, Ismatec, Grevenbroch, Germany) at a flow rate of 1.35 mL min^{-1}. ME2 contained 125 g styrene, 12.6 g BDDA, 0.405 g Dowfax 2A1, 0.401 g SDS, 0.709 g KOH, and 160 g deionized water. After parts of ME2 had been added for over 120 min, the addition was paused for 10 min, and 0.373 g NaPS was added to reinitiate the reaction. After a further pause of 15 min, the addition of ME2 was resumed. 180 min after the initial ME2 addition, the pump was stopped, and the reaction was stirred for an additional hour at 85°C. The reaction mixture was then filtered through a 125 µm nylon sieve and subsequently freeze-dried. For synthesis of the second batch (PS02), the monomer emulsion ME1 consisted of 6.78 g styrene, 0.752 g BDDA, 0.409 g SDS, and 527 g of deionized water. While the emulsion was stirred at 225 rpm, the polymerization was initiated by adding 0.970 g NaPS and 0.139 g NaDS. After 15 min, the second monomer emulsion ME2 was added with the rotary piston pump at a flow rate of 1.35 mL min^{-1}. For the second batch (PS02), the monomer emulsion ME2 contained 124 g styrene, 12.5 g BDDA, 0.411 g Dowfax 2A1, 0.414 g SDS, 0.718 g KOH, and 162 g deionized water. After parts of ME2 had been added for over 120 min, the addition was paused for 10 min, and 0.361 g NaPS was added to reinitiate the reaction. After a further pause of 15 min, the addition of ME2 was resumed. 200 min after the initial ME2 addition, the pump was stopped, and the reaction was stirred for an additional hour at 85°C. The reaction mixture was filtered through a 125 µm nylon sieve and stored as an emulsion in a 1 L PE bottle.

While the freeze-dried Batch 1 was used for the preparation of the inhomogeneous PS/TiO_2 powders, Batch 2, stored in emulsion, was employed to produce the homogeneous powders. Since the synthesis route, particle size analysis (Figure S1d), and thermal decomposition behavior (Figure S6) of both batches were nearly identical, we assume that the two batches exhibit essentially the same behavior in the respective experiments.

5.4 | Preparation of the Pure TiO_2 Powder

Pure TiO_2 powder was prepared by sieving through a 100 µm mesh sieve, followed by drying at 200°C for 12 h in a vacuum oven (Vacutherm, Fisher Scientific, Schwerte, Germany).

5.5 | Preparation of the PS/TiO_2 Composite Powders

Two types of PS/TiO_2 composite powders were prepared. For the preparation of inhomogeneous PS/TiO_2 composite powders, pure TiO_2 powder was prepared as described before. The freeze-dried PS powder PS01 was then manually mixed with the sieved TiO_2 powder in a beaker using a spatula. Two batches with different PS content were prepared, one with 4 wt.% and one with 10 wt.% relative to the total mass of the composite powder. These powders were referred to in the following as 4 wt.% PS/TiO_2 inhom and 10 wt.% PS/TiO_2 inhom, respectively. For the preparation of homogeneous PS/TiO_2 composite powders, the pure TiO_2 powder was dispersed in ultrapure water at a concentration of 150 mg/mL using an ice-cooled ultrasonic bath (Bandelin Sonorex RK 100, Bandelin electronic GmbH & Co. KG, Berlin, Germany). The PS emulsion PS02 (solids content 15.31 wt.%, determined by solvent evaporation in vacuum) was added dropwise to the TiO_2 dispersion under continuous ultrasonication until the desired PS content of either 4 or 10 wt.% (relative to the total mass of the composite powder) was reached. Ultrasonication was resumed for 30 min. The composite dispersion was then freeze-dried to obtain the final powder. These powders were referred to in the following as 4 wt.% PS/TiO_2 hom and 10 wt.% PS/TiO_2 hom, respectively.

5.6 | Particle Size Distribution of TiO_2 Powder

The particle size distribution of the sieved pure TiO_2 powder was determined by static light scattering (SLS) using a Partica LA-960V2 (Horiba, Japan). A few milligrams of the sieved powder were dispersed in ethanol using an ultrasonic bath (Bandelin Sonorex RK 100, Bandelin electronic GmbH & Co. KG, Berlin, Germany). Several drops of the resulting dispersion were transferred into the measurement cell of the instrument. Three measurements were performed in total. The intensities were normalized to the highest value for each measurement. The results are shown in Figure S1.

5.7 | Particle Size Distribution of PS Powder

The hydrodynamic diameter of the PS particles in emulsion was determined by dynamic light scattering (DLS) using a Zetasizer ZS 90 (Malvern Instruments, UK) equipped with a 4 mW, 633 nm HeNe laser. All measurements were performed at 25°C with a scattering angle of 90°. For each sample, five measurements were conducted, with the number of runs automatically determined by the instrument. Data acquisition over 300 size classes and peak analysis were carried out using the Zetasizer Nano software. The intensities were normalized to the highest value for each measurement. The results of this measurement are shown in Figure S1.

5.8 | Scanning Electron Microscopy of the Powders

The morphology of the powders was examined using a Zeiss Sigma 300 VP scanning electron microscope (Zeiss, Oberkochen, Germany). For the pure TiO_2 powder, a drop of an ethanol-based dispersion was placed onto a single-side polished Si wafer (N/Phos, Ø = 100 mm, thickness: 525 ± 25 µm, Si-Mat, Kaufering, Germany). For the composite powders, a few milligrams of powder were applied onto conductive copper carbon tape (Plano GmbH, Wetzlar, Germany). All samples were subsequently sputter-coated with gold using a Cressington Sputter Coater 108 Auto (Tescan GmbH, Dortmund, Germany) using a current of 20 mA at 0.1 mbar for 45 s. SEM images of the pure TiO_2 and the pure PS powder are shown in Figure S1.

5.9 | PAD on PC and Steel Substrates

PAD on PC and stainless steel substrates was carried out using a custom-built research setup, the details of which were described elsewhere [24]. A scheme of the set-up is shown in Figure 1a. Different optimized PAD parameters were used for the different powder/substrate combinations. The parameters used for the samples shown in Figures 3 and 4, respectively, are summarized in Table 2; those for the data shown in Figure 7 are presented in Table 3. It should be noted that, by definition, one scan corresponds to two crossings of the substrate over the nozzle.

5.10 | PAD on Thin and Flexible PET Film

PAD films on thin, flexible PET film (Hostaphan RNK 50) were fabricated using the inhomogeneous 10 wt.% PS/TiO_2 composite powder (Figure 8). First, a 10 × 10 cm^2 PET sheet was fixed with double-sided tape on a steel base plate. Then, the deposition was conducted line-by-line using the PAD parameter set given in Table 4.

5.11 | PAD on Sacrificial Layers

To enable the complete removal of PAD films from the stainless steel substrate, sacrificial layers were applied before the PAD process. The substrates were first roughened using 800-grit sandpaper, rinsed with ethanol, and dried. In parallel, PSS was dissolved in deionized water at room temperature to prepare a 5 wt.% solution. After complete dissolution, 25 wt.% glycerol (relative to the polymer mass) was added, and the solution was allowed to mix at room temperature. A few drops of the PSS-glycerol-water solution were drop-cast onto the stainless steel substrates, which were kept at 100°C and dried for several minutes. PAD experiments on these sacrificial layers were carried out for all investigated powders using the PAD parameter set shown in Table 5. The deposited films were released by immersion in deionized water at 60°C, dissolving the sacrificial layer. The detached films were subsequently rinsed with ethanol, and dried at RT.

5.12 | Thermogravimetric Analysis of the Powders and Films

The composition of the powders was determined by TGA using a TG 209 F1 Libra (Netzsch Holding, Selb, Germany). Measurements were conducted from 30°C to 590°C at a heating rate of 10 K/min. N_2 was used as a protective gas at a flow rate of 20 mL/min, while synthetic air (80% N_2 / 20% O_2) was used as purge gas, also at 20 mL/min. The mass loss was determined from the thermograms. Two samples with an initial mass of at least 10 mg were analyzed per powder. Data processing was carried out using Proteus Thermal Analysis 8.0.1 software (Netzsch Holding, Selb, Germany). To determine the composition of the PAD films, PAD deposits on sacrificial layers were detached as described before. TGA measurements of six deposited films made in three similar deposition experiments, each with two samples in the deposition chamber at the same time, with a total sample mass of a few milligrams, were performed under the same conditions as for the powders.

The evaluation of the TGA curves was carried out in accordance with DIN EN ISO 11358 [74]. In this approach, the temperature of the maximum decomposition rate of the second degradation step (minimum in the dTGA curve) was first determined. The onset and offset temperatures were obtained using the tangent method, with the baseline segments in the TGA curves manually selected around the second degradation step. The onset temperature was defined as the degradation temperature. Data analysis was performed using MATLAB R2022a. A representative example of this evaluation (10 wt.% inhomogeneous film) is shown in Figure S7.

TABLE 2 | PAD parameter set used for the samples for the top-view SEM imaging (Figure 3) and the cross-sectional FIB-SEM imaging (Figure 4).

Parameter	Pure TiO_2	10 wt.% PS/TiO_2 inhom	10 wt.% PS/TiO_2 hom
Nozzle type	Convergent slit nozzle (10 × 0.5 mm)	Convergent slit nozzle (10 × 0.5 mm)	Convergent slit nozzle (10 × 0.5 mm)
Distance nozzle—substrate	10 mm	10 mm	10 mm
Carrier gas type	N_2	N_2	N_2
Carrier gas flow rate	3 slm [a]	3 slm	6 slm
Pressure in the aerosol bottle	98 mbar	98 mbar	167 mbar
Pressure in the deposition chamber	0.59 mbar	0.59 mbar	0.96 mabr
Number of scans	10 [b]	10	25
Scan rate	1 mm s^{-1}	1 mm s^{-1}	5 mm s^{-1}
Frequency of the vibrating platform	400 rpm	400 rpm	400 rpm
Substrate dimensions	225 mm^2	225 mm^2	225 mm^2
Deposited area	100 mm^2	100 mm^2	100 mm^2

[a]standard liters per minute.
[b]1 Scan = 2 crossings.

TABLE 3 | PAD parameter set used for the data shown in Figure 7.

Parameter	Value
Nozzle type	Convergent slit nozzle (10 × 0.5 mm)
Distance nozzle—substrate	1–10 mm
Carrier gas type	N_2
Carrier gas flow rate	1–6 slm
Pressure in the aerosol bottle	47–167 mbar
Pressure in the deposition chamber	0.3–0.96 mabr
Number of scans	2–100 Scans
Scan rate	1–20 mm s^{-1}
Frequency of the vibrating platform	400 rpm
Substrate dimensions	225 mm^2
Deposited area	100 mm^2

5.13 | Laser Scanning Microscopy (LSM) for Film Analysis

The film thickness and surface roughness were analyzed using an OLS4100 laser scanning microscope (LSM, Olympus GmbH, Germany) with a dual confocal scanning system equipped with a 405 nm semiconductor laser. The substrates were mounted on a flat sample holder using double-sided adhesive tape. Scans for the composite films were performed with the MPLAPONLEXT x20 objective lens (Olympus GmbH, Germany) and no additional optical zoom across the entire film width (substrate-film-substrate) using individual image fields of at least 600 × 600 µm stitched together to capture the complete height profile of both substrate and film. Scans for the pure TiO_2 films were performed with the same objective across the edge of the film on one side in the same way. Surface corrections in the x- and y-directions were applied using the Olympus OLS4100 3.1.5.9 software to compensate for substrate curvature. The data were further processed in Matlab R2024b. Substrate and film regions were segmented by thresholding, and fixed evaluation areas were defined: 500 × 600 $µm^2$ for the substrate and 8000 × 600 $µm^2$ for the film (4000 × 600 $µm^2$ in the case of pure TiO_2). The mean height of the substrate regions was subtracted from both the film and substrate regions to level the data in the evaluation areas. Profiles were tilt-corrected afterward. Based on the resulting data, the mean film profile was determined, and the average film thickness, film width, and roughness parameters were evaluated separately for substrate and film.

TABLE 4 | PAD parameter set used for the films made on PET film (Figure 8).

Parameter	Value
Nozzle type	Convergent slit nozzle (10 × 0.5 mm)
Distance nozzle—substrate	2 mm
Carrier gas type	N_2
Carrier gas flow rate	6 slm
Pressure in the aerosol bottle	167 mbar
Pressure in the deposition chamber	0.96 mbar
Number of scans	2
Scan rate	5 mm s^{-1}
Frequency of the vibrating platform	400 rpm
Substrate dimensions	100 cm^2
Deposited area	100 cm^2

TABLE 5 | PAD parameter set used for the deposition on sacrificial layers for TGA (Figure 6).

Parameter	10 wt.% PS/TiO_2 inhom	Others
Nozzle type	Convergent slit nozzle (10 × 0.5 mm)	Convergent slit nozzle (10 × 0.5 mm)
Distance nozzle—substrate	2 mm	2 mm
Carrier gas type	N_2	N_2
Carrier gas flow rate	6 slm	3 slm
Pressure in the aerosol bottle	167 mbar	98 mbar
Pressure in the deposition chamber	0.96 mbar	0.59 mbar
Number of scans	25	25
Scan rate	5 mm s^{-1}	5 mm s^{-1}
Frequency of the vibrating platform	400 rpm	400 rpm
Substrate dimensions	225 mm^2	225 mm^2
Deposited area	100 mm^2	100 mm^2

5.14 | Calculating Deposition Efficiency (DE) and Deposition Rate (DR) for Film Analysis

Deposition efficiency (DE) was calculated according to Equation 1.

$$DE = \frac{m_f}{m_p\left(t_{deposition}\right)} \cdot 100\% \tag{1}$$

where m_f is the mass of the deposited film, and m_p is the mass of powder discharged during the effective deposition time $t_{deposition}$. Effective deposition time $t_{deposition}$ was determined using Equation 2.

$$t_{deposition} = \frac{2 \cdot n_{scans} \cdot b_f}{v_{scan}} \tag{2}$$

where n_{scans} is the number of scans performed during the process, b_f is the width of the film, and v_{scan} is the scan velocity. The mass of the powder discharged during deposition time, m_p, was calculated as powder discharge rate, which is the powder mass in the aerosol chamber before and after the process, Δm_p, over the process time $t_{process}$, multiplied with $t_{deposition}$, as shown in Equation 3.

$$m_p = \frac{\Delta m_p}{t_{process}} \cdot t_{deposition} \tag{3}$$

The values for m_f are calculated using Equation 4.

$$m_f = \rho_f \cdot A_f \cdot h_f \tag{4}$$

where A_f is the film area, h_f the average film thickness measured with LSM, and ρ_f the film density. For the film density ρ_f, values were determined assuming a simple rule of mixture based on the bulk densities of PS (ρ_{PS} = 1.04 g cm^{-3}) and TiO_2 (rutile, ρ_{TiO_2} = 4.24 g cm^{-3}) according to Equation 5.

$$\rho_f = \frac{1}{\left(\frac{x_{PS}}{\rho_{PS}}\right) + \left(\frac{x_{TiO_2}}{\rho_{TiO_2}}\right)} \tag{5}$$

with x_{PS} as the mass loss in mass percent from Figure 6b and $x_{TiO_2} = 100 - x_{PS}$. Deposition rate (DR) was calculated using Equation 6:

$$DR = \frac{h_f}{t_{deposition}} \quad (6)$$

5.15 | Focused Ion Beam (FIB)-SEM Cross-Sections for Film Microstructure

Local cross sections for inspecting the film microstructure were performed using either a Helios Nanolab600 (FEI, Hillsboro, Oregon, USA) equipped with a gallium focused ion beam or Helios PFIB G4 CXe (Thermo Fisher Scientific, Waltham, Massachusetts, USA) equipped with a focused xenon ion beam. To avoid charging effects, samples were sputter-coated with ~10 nm palladium using a K950x (Emitech, Ashford, UK) evaporator with sputter head attachment at a pressure of 0.02 mbar and a discharge current of 20–25 mA for 2 min. Inside the FIB, regions of interest close to the center of the coating were protected with a platinum-based beam-assisted deposition of 1–5 µm in a two-step process. First, a thin layer was deposited using the electron beam to avoid ion beam damage to the sample. Second, a thicker layer was deposited using the ion beam, exploiting the higher deposition rate. Actual thickness was adapted to the expected total thickness of the PAD film. FIB cross-sections were then carried out using beam currents starting at 21 or 65 nA for coarse trenching, followed by decreasing currents down to 1 nA for fine polishing. Imaging was done using the electron beam at 5 kV acceleration voltage and 86 pA beam current using the Everhart–Thornley secondary electron detector. No obvious signs of ion beam damage to the microstructure morphology, e.g. bubbling or loss of shape could be observed in any of the samples.

5.16 | X-Ray Diffraction Measurements for Film Microstructure

Powder X-ray diffraction (PXRD) patterns of the powders and PAD coatings were recorded at room temperature on a D8-A25-Advance diffractometer (Bruker, Karlsruhe, Germany) in Bragg-Brentano θ-θ-geometry (goniometer radius 280 mm) with Cu K_α radiation ($\lambda = 154.0596$ pm). A 12 µm Ni foil working as a K_β filter and a variable divergence slit were mounted at the primary beam side. A LYNXEYE detector with 192 channels was used at the secondary beam side. Experiments were carried out in a 2θ range of 6°–130° with a step size of 0.013° and a total scan time of 1 h. The samples were placed on zero-background silicon sample holders to avoid background contributions from the typical metal sample holders. The data was refined using the Rietveld method [75, 76] using the program package TOPAS 5.0 [77] applying the fundamental parameter approach.

Acknowledgements

This work was funded by the German Research Foundation (Heisenberg program, LI 1714/9-1). It made use of resources of the Correlative Microscopy and Tomography (CoMiTo) core facility at Saarland University, including the PFIB/SEM funded by the German Research Foundation (415217285). Further instrumentation and technical assistance for this work were provided by the Service Center X-ray Diffraction, which is financially supported by the Saarland University and the German Research Foundation (INST 256/349-1). M.G. and S.V. acknowledge the partial financial support from the German Research Foundation (DFG) through the priority program (SPP 2451) and the OPAL-Bac project (GA 2169/11-1 and SCHN 945/6-1). The authors thank Dr. Oliver Janka for the technical and analytical support with the X-ray diffraction measurement and data evaluation, and the Chair of Functional Materials (Prof. Dr.-Ing. Frank Mücklich, Saarland University) for access to the LSM instrument, and Jonas Dörr and Lukas Siegwardt (both Chair of Polymer Materials of Prof. Dr. M.G., Saarland University) for performing the TGA measurements and for helping with polystyrene particle synthesis. Pascal Paul (Helmholtz Institute for Pharmaceutical Research, Saarland University) is acknowledged for assistance with particle size distribution measurements. Prof. Dr. Ralf Moos and his team (University of Bayreuth, Bayreuth, Germany) are most gratefully acknowledged for generously sharing their PAD experience, and for helpful input for the experiments, thus making the world of PAD accessible for us newcomers. AI tools were used for assistance with literature search, translations, and proof-reading in the context of this research.

Open access funding enabled and organized by Projekt DEAL.

Funding

German Research Foundation, grant IDs: LI 1714/9-1, 415217285, INST 256/349-1, SPP 2451, GA 2169/11-1 and SCHN 945/6-1.

Conflicts of Interest

The authors declare no conflicts of interest.

Data Availability Statement

The data that support the findings of this study are available from the corresponding author upon reasonable request.

References

1. V. P. Singh, A. Sil, and R. Jayaganthan, "A Study on Sliding and Erosive Wear Behaviour of Atmospheric Plasma Sprayed Conventional and Nanostructured Alumina Coatings," *Materials & Design* 32 (2011): 584–591.

2. G. Ma, S. Yan, D. Wu, Q. Miao, M. Liu, and F. Niu, "Microstructure Evolution and Mechanical Properties of Ultrasonic Assisted Laser Clad Yttria Stabilized Zirconia Coating," *Ceramics International* 43 (2017): 9622–9629.

3. J. Mukherjee, S. Chakraborty, S. Chakravarty, A. Ranjan, and P. K. Das, "Mechanical and Tribological Properties of Silicon Carbide Coating on Inconel Alloy from Liquid Pre-ceramic Precursor," *Ceramics International* 40 (2014): 6639–6645.

4. A. Fox and T. Clyne, "Oxygen Transport by Gas Permeation through the Zirconia Layer in Plasma Sprayed Thermal Barrier Coatings," *Surface and Coatings Technology* 184 (2004): 311–321.

5. L. Wang, Y. Wang, X. Sun, J. He, Z. Pan, and C. Wang, "Thermal Shock Behavior of 8YSZ and Double-ceramic-layer La2Zr2O7/8YSZ Thermal Barrier Coatings Fabricated by Atmospheric Plasma Spraying," *Ceramics International* 38 (2012): 3595–3606.

6. Z. Xu, S. He, L. He, R. Mu, G. Huang, and X. Cao, "Novel Thermal Barrier Coatings Based on La2(Zr0.7Ce0.3)2O7/8YSZ Double-ceramic-layer Systems Deposited by Electron Beam Physical Vapor Deposition," *Journal of Alloys and Compounds* 509 (2011): 4273–4283.

7. T. Olding, M. Sayer, and D. Barrow, "Ceramic Sol–gel Composite Coatings for Electrical Insulation," *Thin Solid Films* 398-399 (2001): 581–586.

8. M. Mohammadian Bajgiran, M. Rezvani Rad, A. McDonald, and C. Moreau, "Microstructure, Phase and Dielectric Strength of Ther-

mally Sprayed Alumina Layers in Coating-Based Heating Systems," *International Journal of Applied Ceramic Technology* 18 (2021): 1641–1656.

9. M. Huang, Y. Tian, N. Kong, et al., "Coating Dense Silicon Carbide Layer on Artificial Graphites to Achieve Synergistically Enhanced Thermal Conductivity and Electronic Insulation of Polymer Composites," *Journal of Applied Polymer Science* 140 (2023): 53983.

10. S. Tiwari, M. Tripathi, and R. Singh, "Electrochemical Behavior of Zirconia Based Coatings on Mild Steel Prepared by Sol–gel Method," *Corrosion Science* 63 (2012): 334–341.

11. A.-M. Lazar, W. P. Yespica, S. Marcelin, et al., "Corrosion Protection of 304L Stainless Steel by Chemical Vapor Deposited Alumina Coatings," *Corrosion Science* 81 (2014): 125–131.

12. H. Qian, Z. Xu, S. Chen, Y. Liu, and D. Yan, "Silicon Carbide/Enamel Composite Coatings for Steel Corrosion Protection: Microstructure, Thermal Expansion Behavior, and Anti-corrosion Performance," *Surface and Coatings Technology* 434 (2022): 128172.

13. J.-K. Pi, G.-P. Wu, H.-C. Yang, C. G. Arges, and Z.-K. Xu, "Separators with Biomineralized Zirconia Coatings for Enhanced Thermo- and Electro-Performance of Lithium-Ion Batteries," *ACS Applied Materials & Interfaces* 9 (2017): 21971–21978.

14. J.-H. Ha, S. Z. A. Bukhari, J. Lee, I.-H. Song, and C. Park, "Preparation Processes and Characterizations of Alumina-coated Alumina Support Layers and Alumina-coated Natural Material-based Support Layers for Microfiltration," *Ceramics International* 42 (2016): 13796–13804.

15. A. Jan, M. Nijboer, G. Qin, M. Luiten-Olieman, L. C. Rietveld, and S. G. Heijman, "Silicon Carbide Coated Alumina Tight-ultrafiltration Membrane Prepared by Low-pressure Chemical Vapor Deposition for Sulphate Ion Retention," *Desalination* 613 (2025): 119085.

16. H. Gollwitzer, M. Haenle, W. Mittelmeier, F. Heidenau, and N. Harrasser, "A Biocompatible Sol–gel Derived Titania Coating for Medical Implants with Antibacterial Modification by Copper Integration," *AMB Express* 8 (2018): 24.

17. G. S. Kaliaraj, V. Vishwakarma, and A. K. Kirubaharan, "Biocompatible Zirconia-Coated 316 Stainless Steel with Anticorrosive Behavior for Biomedical Application," *Ceramics International* 44 (2018): 9780–9786.

18. T. Matijosius, N. Bakute, J. Padgurskas, et al., "Corrosion and Biocompatibility Studies of Bioceramic Alumina Coatings on Aluminum Alloy 6082," *ACS Applied Materials & Interfaces* 17 (2025): 24901–24917.

19. L. J. Bonderer, P. W. Chen, P. Kocher, and L. J. Gauckler, "Free-Standing Ultrathin Ceramic Foils," *Journal of the American Ceramic Society* 93 (2010): 3624–3631.

20. M. Hashizume and T. Kunitake, "Preparation and Functionalization of Self-supporting (polymer/metal oxide) Composite Ultrathin Films," *Riken Review* (2001): 36–39.

21. L. Gao, H. Guo, L. Wei, C. Li, S. Gong, and H. Xu, "Microstructure and Mechanical Properties of Yttria Stabilized Zirconia Coatings Prepared by Plasma Spray Physical Vapor Deposition," *Ceramics International* 41 (2015): 8305–8311.

22. I. Zhitomirsky, "Cathodic Electrodeposition of Ceramic and Organoceramic Materials. Fundamental Aspects," *Advances in Colloid and Interface Science* 97 (2002): 279–317.

23. J. Akedo, "Aerosol Deposition of Ceramic Thick Films at Room Temperature: Densification Mechanism of Ceramic Layers," *Journal of the American Ceramic Society* 89 (2006): 1834–1839.

24. D. Hanft, J. Exner, M. Schubert, T. Stöcker, P. Fuierer, and R. Moos, "An Overview of the Aerosol Deposition Method: Process Fundamentals and New Trends in Materials Applications," *Journal of Ceramic Science and Technology* 6 (2015): 147–182.

25. M. Schubert, D. Hanft, T. Nazarenus, et al., "Powder Aerosol Deposition Method — Novel Applications in the Field of Sensing and Energy Technology," *Functional Materials Letters* 12 (2019): 1930005.

26. J. Akedo, "Room Temperature Impact Consolidation and Application to Ceramic Coatings: Aerosol Deposition Method," *Journal of the Ceramic Society of Japan* 128 (2020): 101–116.

27. L.-S. Wang, H.-F. Zhou, K.-J. Zhang, et al., "Effect of the Powder Particle Structure and Substrate Hardness during Vacuum Cold Spraying of Al 2 O 3," *Ceramics International* 43 (2017): 4390–4398.

28. M. Lebedev and J. Akedo, "Effect of Thickness on the Piezoelectric Properties of Lead Zirconate Titanate Films Fabricated by Aerosol Deposition Method," *Japanese Journal of Applied Physics* 41 (2002): 6669.

29. K. Mihara, T. Hoshina, H. Takeda, and T. Tsurumi, "Controlling Factors of Film-thickness in Improved Aerosol Deposition Method," *Journal of the Ceramic Society of Japan* 117 (2009): 868–872.

30. D.-W. Lee, H.-J. Kim, and S.-M. Nam, "Lee Al2O3 Films on Cu Substrates Using the Aerosol Deposition Method," *Journal of the Korean Physical Society* 57 (2010): 1115–1121.

31. E. Fuchita, E. Tokizaki, and Y. Sakka, "Formation of Zirconia Films by the Aerosol Gas Deposition Method," *Journal of the Ceramic Society of Japan* 118 (2010): 767–770.

32. H.-J. Kim and S.-M. Nam, "Powder Preparation in Aerosol Deposition for Al2O3-polyimide Composite Thick Films," *Electronic Materials Letters* 8 (2012): 65–70.

33. K. Naoe, K. Sato, and M. Nishiki, "Effect of Process for Producing Al₂O₃ Particles on Deposition Efficiency in Aerosol Deposition Method," *Journal of the Ceramic Society of Japan* 122 (2014): 110–116.

34. Z. Yao, C. Wang, Y. Li, H.-K. Kim, and N.-Y. Kim, "Effects of Starting Powder and Thermal Treatment on the Aerosol Deposited BaTiO3 Thin Films toward Less Leakage Currents," *Nanoscale Research Letters* 9 (2014): 435.

35. J. Exner, M. Hahn, M. Schubert, D. Hanft, P. Fuierer, and R. Moos, "Powder Requirements for Aerosol Deposition of Alumina Films," *Advanced Powder Technology* 26 (2015): 1143–1151.

36. J. Exner, M. Schubert, D. Hanft, J. Kita, and R. Moos, "How to Treat Powders for the Room Temperature Aerosol Deposition Method to Avoid Porous, Low Strength Ceramic Films," *Journal of the European Ceramic Society* 39 (2019): 592–600.

37. D. Hanft, M. Bektas, and R. Moos, "Powder Pre-Treatment for Aerosol Deposition of Tin Dioxide Coatings for Gas Sensors," *Materials* 11 (2018): 1342.

38. S. Baba, J. Akedo, M. Tsukamoto, and N. Abe, "Effect of Carrier Gas Species on Ferroelectric Properties of PZT/Stainless-Steel Fabricated by CO 2 Laser-Assisted Aerosol Deposition," *Journal of the American Ceramic Society* 89 (2006): 1736–1738.

39. G.-J. Yang, C.-J. Li, K.-X. Liao, X.-L. He, S. Li, and S.-Q. Fan, "Influence of Gas Flow during Vacuum Cold Spraying of Nano-porous TiO2 Film by Using Strengthened Nanostructured Powder on Performance of Dye-sensitized Solar Cell," *Thin Solid Films* 519 (2011): 4709–4713.

40. F. Cao, H. Park, J. Heo, J. Kwon, and C. Lee, "Effect of Process Gas Flow on the Coating Microstructure and Mechanical Properties of Vacuum Kinetic-Sprayed TiN Layers," *Journal of Thermal Spray Technology* 22 (2013): 1109–1119.

41. M. Schubert, J. Exner, and R. Moos, "Influence of Carrier Gas Composition on the Stress of Al2O3 Coatings Prepared by the Aerosol Deposition Method," *Materials* 7 (2014): 5633–5642.

42. K. Naoe, M. Nishiki, and A. Yumoto, "Relationship between Impact Velocity of Al2O3 Particles and Deposition Efficiency in Aerosol Deposition Method," *Journal of Thermal Spray Technology* 22 (2013): 1267–1274.

43. J. Kwon, H. Park, I. Lee, and C. Lee, "Effect of Gas Flow Rate on Deposition Behavior of Fe-based Amorphous Alloys in Vacuum Kinetic Spray Process," *Surface and Coatings Technology* 259 (2014): 585–593.

44. T. P. Mishra, R. Singh, R. Mücke, et al., "Influence of Process Parameters on the Aerosol Deposition (AD) of Yttria-Stabilized Zirconia Particles," *Journal of Thermal Spray Technology* 30 (2021): 488–502.

45. P. Glosse, S. Denneler, O. Stier, and R. Moos, "Investigation of the Powder Aerosol Deposition Method Using Shadowgraph Imaging," *Materials* 14 (2021): 2502.

46. C.-W. Kim, J.-H. Choi, H.-J. Kim, D.-W. Lee, C.-Y. Hyun, and S.-M. Nam, "Effects of Interlayer Roughness on Deposition Rate and Morphology of Aerosol-deposited Al2O3 Thick Films," *Ceramics International* 38 (2012): 5621–5627.

47. D.-W. Lee, H.-J. Kim, Y.-N. Kim, M.-S. Jeon, and S.-M. Nam, "Substrate Hardness Dependency on Properties of Al2O3 Thick Films Grown by Aerosol Deposition," *Surface and Coatings Technology* 209 (2012): 160–168.

48. M. Schubert, M. Hahn, J. Exner, J. Kita, and R. Moos, "Effect of Substrate Hardness and Surface Roughness on the Film Formation of Aerosol-deposited Ceramic Films," *Functional Materials Letters* 10 (2017): 1750045.

49. S.-Q. Fan, C.-J. Li, C.-X. Li, G.-J. Liu, G.-J. Yang, and L.-Z. Zhang, "Preliminary Study of Performance of Dye-Sensitized Solar Cell of Nano-TiO₂ Coating Deposited by Vacuum Cold Spraying," *Materials Transactions* 47 (2006): 1703–1709.

50. J.-J. Choi, B.-D. Hahn, J. Ryu, W.-H. Yoon, B.-K. Lee, and D.-S. Park, "Preparation and Characterization of Piezoelectric Ceramic–polymer Composite Thick Films by Aerosol Deposition for Sensor Application," *Sensors and Actuators A: Physical* 153 (2009): 89–95.

51. H. Kim, Y. Yoon, J. Kim, and S. Nam, "Application of Al2O3-based Polyimide Composite Thick Films to Integrated Substrates Using Aerosol Deposition Method," *Materials Science and Engineering: B* 161 (2009): 104–108.

52. H.-J. Kim, Y.-H. Kim, S.-M. Nam, Y. J. Yoon, and J.-H. Kim, "Calculation of Al2O3 Contents in Al2O3-PTFE Composite Thick Films Fabricated by Using the Aerosol Deposition," *Journal of the Korean Physical Society* 57 (2010): 1086–1091.

53. G. Han, J. Ryu, W. H. Yoon, J. J. Choi, B. D. Hahn, and D. S. Park, "Effect of Film Thickness on the Piezoelectric Properties of Lead Zirconate Titanate Thick Films Fabricated by Aerosol Deposition," *Journal of the American Ceramic Society* 94 (2011): 1509–1513.

54. B.-D. Hahn, D.-S. Park, J.-J. Choi, et al., "Aerosol Deposition of Hydroxyapatite–chitosan Composite Coatings on Biodegradable Magnesium Alloy," *Surface and Coatings Technology* 205 (2011): 3112–3118.

55. Y.-H. Kim, H.-J. Kim, J.-H. Koh, J.-G. Ha, Y.-H. Yun, and S.-M. Nam, "Fabrication of BaTiO3-PTFE Composite Film for Embedded Capacitor Employing Aerosol Deposition," *Ceramics International* 37 (2011): 1859–1864.

56. J.-J. Choi, J.-H. Choi, J. Ryu, et al., "Low-temperature Fabrication of Nano-structured Porous (La,Sr)(Co,Fe)O3− Cathodes by Aerosol Deposition," *Journal of Alloys and Compounds* 545 (2012): 186–189.

57. S. H. Cho, Y. J. Yoon, H. T. Kim, et al., "Growth of Al2O3–PTFE Composite Film at Room Temperature by Aerosol Deposition Method," *Ceramics International* 38 (2012): S131–S134.

58. H.-J. Kim, Y.-H. Kim, J.-W. Lee, S.-M. Nam, Y. J. Yoon, and J.-H. Kim, "Residual Stress Relief in Al₂O₃–Poly-Tetra-Fluoro-Ethylene Hybrid Thick Films for Integrated Substrates Using Aerosol Deposition," *Journal of Nanoelectronics and Optoelectronics* 7 (2012): 287–291.

59. H.-J. Kim and S.-M. Nam, "Synthesis, Structure, and Photovoltaic Property of a Nanocrystalline 2H Perovskite-type Novel Sensitizer (CH3CH2NH3)PbI3," *Nanoscale Research Letters* 7 (2012): 353.

60. H.-J. Kim, O.-Y. Kwon, C.-I. Jang, et al., "Room-temperature Growth of Ni-Zn-Cu Ferrite/PTFE Composite Thick Films on PET via Aerosol Deposition," *Electronic Materials Letters* 9 (2013): 805–807.

61. H.-J. Kim, S.-M. Nam, and J.-H. Koh, "Fe–Si–Cr/PTFE Magnetic Composite Thick Films on Polyethylene Terephthalate Sheets for Near Field Communications by Aerosol Deposition," *Journal of Nanoscience and Nanotechnology* 14 (2014): 7915–7918.

62. S. H. Cho and Y. J. Yoon, "Growth of BaTiO3-PVDF Composite Thick Films by Using Aerosol Deposition," *Journal of the Korean Physical Society* 68 (2016): 340–344.

63. I. S. Kim, M. Y. Cho, Y. Jeong, et al., "Aerosol-Deposited Al 2 O 3 /PTFE Hydrophobic Coatings with Adjustable Transparency," *Journal of the American Ceramic Society* 104 (2021): 1716–1725.

64. S.-J. Yun, J.-H. Kim, H.-A. Cha, et al., "Low Thermal Conductivity and High Durability Porous Thermal Insulation Coating via Room–temperature Spray Coating Process," *Journal of the Korean Physical Society* 61 (2023): 142–152.

65. M.-Y. Cho, S.-J. Park, S.-M. Kim, et al., "Hydrophobicity and Transparency of Al2O3-based Poly-tetra-fluoro-ethylene Composite Thin Films Using Aerosol Deposition," *Ceramics International* 44 (2018): 16548–16555.

66. O.-Y. Kwon, H.-J. Na, H.-J. Kim, D.-W. Lee, and S.-M. Nam, "Effects of Mechanical Properties of Polymer on Ceramic-polymer Composite Thick Films Fabricated by Aerosol Deposition," *Nanoscale Research Letters* 7 (2012): 1–8.

67. S. Kim, M. Y. Cho, I. S. Kim, et al., "Solvent-Free Aerosol Deposition for Highly Luminescent and Thermally Stable Perovskite-Ceramic Nanocomposite Film," *Advanced Materials Interfaces* 6 (2019): 1900359.

68. H. Park, H. Kwon, J. Kim, and C. Lee, "Shock Absorption Effect on Particle Fragmentation and Microstructural Features of Vacuum-Kinetic-Sprayed Al2O3 Film on Polycarbonate Substrate," *Journal of Thermal Spray Technology* 30 (2021): 558–570.

69. E. K. Riga, E. Gillies, and K. Lienkamp, "Self-Regenerating Antimicrobial Polymer Surfaces via Multilayer-Design—Sequential and Triggered Layer Shedding under Physiological Conditions," *Advanced Materials Interfaces* 6 (2019): 12.

70. Z. Deng and K. Lienkamp, "Self-Regenerating of Functional Polymer Surfaces by Triggered Layer Shedding Using a Stimulus-Responsive Poly(urethane)," *Macromolecular Chemistry and Physics* 222 (2021): 2100127.

71. N. H. Khansur, U. Eckstein, Y. Li, D. A. Hall, J. Kaschta, and K. G. Webber, "Revealing the Effects of Aerosol Deposition on the Substrate-Film Interface Using NaCl Coating," *Journal of the American Ceramic Society* 102 (2019): 5763–5771.

72. T. Goto, Y. Matsubayashi, and J. Akedo, "Ceramic Coating on Rubber by Aerosol Deposition with Cryogenic Substrate Cooling," *Ceramics International* 50 (2024): 892–896.

73. M. N. E. A. Al Nasim and D.-M. Chun, "Substrate-dependent Deposition Behavior of Graphite Particles Dry-sprayed at Room Temperature Using a Nano-particle Deposition System," *Surface and Coatings Technology* 309 (2017): 172–178.

74. International Organization of Standardization, DIN EN ISO 11358: Plastics – Thermogravimetry (TG) of polymers – Part 1: General principles (2014), https://www.iso.org/standard/79999.html.

75. H. M. Rietveld, "Line Profiles of Neutron Powder-diffraction Peaks for Structure Refinement," *Acta Crystallographica* 22 (1967): 151–152.

76. H. M. Rietveld, "A Profile Refinement Method for Nuclear and Magnetic Structures," *Journal of Applied Crystallography* 2 (1969): 65–71.

77. Bruker AXS Inc., Topas, Karlsruhe (Germany) (2014), https://www.bruker.com/en/products-and-solutions/diffractometers-and-x-ray-microscopes/x-ray-diffractometers/diffrac-suite-software/diffrac-topas.html.

Supporting Information

Additional supporting information can be found online in the Supporting Information section.

Supporting file 1: admi70380-sup-0001-SuppMat.docx.